

THE ORBIT AND DYNAMICAL MASS OF POLARIS: OBSERVATIONS WITH THE CHARA ARRAY

NANCY REMAGE EVANS

Smithsonian Astrophysical Observatory, MS 4, 60 Garden St., Cambridge, MA 02138; nevens@cfa.harvard.edu

GAIL H. SCHAEFER

CHARA Array of Georgia State University, Mount Wilson, CA 91023

ALEXANDRE GALLENNE

Instituto de Astrofísica, Departamento de Ciencias Físicas, Facultad de Ciencias Exactas, Universidad Andrés Bello, Fernández Concha 700, Las Condes, Santiago, Chile and French-Chilean Laboratory for Astronomy, IRL 3386, CNRS, Casilla 36-D, Santiago, Chile

GUILLERMO TORRES

Smithsonian Astrophysical Observatory, 60 Garden St., Cambridge, MA 02138

ELLIOTT P. HORCH

Department of Physics, Southern Connecticut State Univ, 501 Crescent Street, New Haven, CT 06515

RICHARD I ANDERSON

Institute of Physics, École Polytechnique Fédérale de Lausanne (EPFL), Observatoire de Sauverny, 1290 Versoix, Switzerland

JOHN D. MONNIER

University of Michigan, Department of Astronomy, 1085 S. University, Ann Arbor, MI 48109

RACHAEL M. ROETTENBACHER

University of Michigan, Department of Astronomy, 1085 S. University, Ann Arbor, MI 48109

FABIEN BARON

Center for High Angular Resolution Astronomy and Department of Physics and Astronomy, Georgia State University, P.O. Box 5060, Atlanta, GA 30302-5060

NARSIREDDY ANUGU

CHARA Array of Georgia State University, Mount Wilson, CA 91023

JAMES W. DAVIDSON, JR.

Department of Astronomy, Univ. of Virginia, 530 McCormick Rd., Charlottesville, VA 22904

PIERRE KERVELLA

LESIA, Observatoire de Paris, Université PSL, CNRS, Sorbonne Université, Université Paris Cité, 5 place Jules Janssen, 92195 Meudon, France

GARANCE BRAS

LESIA, Observatoire de Paris, Université PSL, CNRS, Sorbonne Université, Université Paris Cité, 5 place Jules Janssen, 92195 Meudon, France

CHARLES PROFFITT

Space Telescope Science Institute, 3700 San Martin Drive, Baltimore, MD 21218

ANTOINE MÉRAND

European Southern Observatory, Karl-Schwarzschild-Str. 2, 85748 Garching, Germany

MARGARITA KAROVSKA

Smithsonian Astrophysical Observatory, MS 4, 60 Garden St., Cambridge, MA 02138

JEREMY JONES

Center for High Angular Resolution Astronomy and Department of Physics and Astronomy, Georgia State University, P.O. Box 5060, Atlanta, GA 30302-5060

CYPRIEN LANTHERMANN

CHARA Array of Georgia State University, Mount Wilson, CA 91023

STEFAN KRAUS

University of Exeter, School of Physics and Astronomy, Astrophysics Group, Stocker Road, Exeter, EX4 4QL, UK

ISABELLE CODRON

University of Exeter, School of Physics and Astronomy, Astrophysics Group, Stocker Road, Exeter, EX4 4QL, UK

HOWARD E. BOND

Department of Astronomy & Astrophysics, Pennsylvania State University, University Park, PA, 16802, USA and Space Telescope Science Institute, 3700 San Martin Dr., Baltimore, MD 21218, USA

GIORDANO VIVIANI

Institute of Physics, École Polytechnique Fédérale de Lausanne (EPFL), Observatoire de Sauverny, 1290 Versoix, Switzerland

ABSTRACT

The 30 year orbit of the Cepheid Polaris has been followed with observations by the CHARA Array (Center for High Angular Resolution Astronomy) from 2016 through 2021. An additional measure-

ment has been made with speckle interferometry at the Apache Point Observatory. Detection of the companion is complicated by its comparative faintness—an extreme flux ratio. Angular diameter measurements appear to show some variation with pulsation phase. Astrometric positions of the companion were measured with a custom grid-based model-fitting procedure and confirmed with the CANDID software. These positions were combined with the extensive radial velocities discussed by Torres (2023) to fit an orbit. Because of the imbalance of the sizes of the astrometry and radial velocity datasets, several methods of weighting are discussed. The resulting mass of the Cepheid is $5.13 \pm 0.28 M_{\odot}$. Because of the comparatively large eccentricity of the orbit (0.63), the mass derived is sensitive to the value found for the eccentricity. The mass combined with the distance shows that the Cepheid is more luminous than predicted for this mass from evolutionary tracks. The identification of surface spots is discussed. This would give credence to the identification of photometric variation with a period of approximately 120 days as a rotation period. Polaris has some unusual properties (rapid period change, a phase jump, variable amplitude, unusual polarization). However, a pulsation scenario involving pulsation mode, orbital periastron passage (Torres 2023), and low pulsation amplitude can explain these characteristics within the framework of pulsation seen in Cepheids.

Keywords: stars: masses Cepheids: Polaris: binaries; stars:massive; stars: variable

1. INTRODUCTION

The importance of Cepheid variable stars as the first step in the cosmological distance scale has been emphasized recently in the discussion of the tension between the Hubble constant H_0 from Cepheids and Type Ia supernovae and that from the early universe based on *Planck* CMB observations (Riess et al. 2021).

Another property of Cepheids, their masses, provides pivotal tests of stellar evolution and predictions of the production of end-stage objects such as neutron stars. In stellar evolution calculations, the luminosity at the Cepheid stage depends on main-sequence core convective overshooting and rotation in Cepheid progenitors (B stars; Anderson et al. 2014) and also mass loss (see eg. Neilson et al. 2013). Asteroseismology from space-based observations is revolutionizing stellar evolution calculations by providing information about the internal structure of stars (Kurtz 2022). Comparing the Mass-Luminosity (ML) relation from calculations with observed quantities is an important test. The persistent “Cepheid mass problem” (the disagreement between masses inferred from evolutionary tracks and from pulsation calculations) has been reduced to about 10% (Bono et al. 2001, Neilson et al. 2011) but still remains. While calibration of Cepheid luminosities will be significantly improved in the final *Gaia* release, their masses can only be measured directly in binary systems, and hence only a limited number are available, one of which is Polaris.

A further motivation for determining the masses of Milky Way (MW) Cepheids as accurately as possible is that six Cepheids have been found to be members of eclipsing binaries in the Large Magellanic Cloud (LMC; Pilecki et al. 2018, 2021), so comparison between the ML relations for the metallicities of the MW and the LMC can now be made.

Cepheids have typical masses of about 4–5 M_{\odot} , but the longest-period Cepheids may be as massive as $\sim 11 M_{\odot}$ (Anderson et al. 2014). Most Cepheids are fated to become white dwarfs; however, the most massive may become supernovae, and end their lives as neutron stars. As an example of the importance of the calibration of the Cepheid ML relation, V1334 Cyg is the Cepheid in the MW which has the most accurate dynamical mass (accurate to 3%; Gallenne et al. 2018). This mass is smaller than predicted by evolutionary tracks. This means that the fraction of Cepheids which are massive enough to become neutron stars could be smaller than expected, leading to implications for the frequency of neutron stars.

Mass determination starts with a radial velocity orbit and pulsation curve for a binary containing a Cepheid. At the present time several new capabilities are available which make it possible to directly measure model-independent, dynamical masses for Cepheids using this orbit. Interferometry has resolved a number of systems, providing the semi-major axis, $a = a_1 + a_2$, and the inclination, i . CHARA (Center for High Angular Resolution Astronomy) Array and the Very Large Telescope Interferometer (VLTI) make it possible to reach stars in both hemispheres. In addition, high-resolution spectra in the ultraviolet (UV) from *Hubble Space Telescope (HST)* allow the orbital radial-velocity amplitude of hot companions of Cepheids to be measured. The *Gaia* spacecraft can provide both distances and proper motions. Astrometry is modeled by a sum of constant proper motion and an astrometric orbit, including the inclination. Final versions of proper motions and distances will not be available **for Cepheids generally** until the *Gaia* DR4 data release which includes orbital solutions in the astrometry **routinely**.

The accuracy of inputs from any of these measurements depends on many characteristics of the star: brightness,

orbital period, inclination, and separation, distance, and mass ratio of the components. This means that each Cepheid system is unique and has to be analyzed independently. The system under discussion here (Polaris), for instance, has a comparatively low mass companion. It is not possible to measure a velocity of the companion with *HST* UV spectra. It is also too bright to be accurately measured by *Gaia*, so the distance determination depends on a third star in the system, as discussed below. However, because it is the nearest Cepheid, and has a long period orbit, the system has been resolved by *HST*, CHARA and speckle interferometry at APO. The long orbital period, however, results in a low velocity amplitude and the need to make use of a combination of radial velocities from many instruments. Both the low orbital velocity amplitude and the use of data from many sources are challenges for the basic orbit determination, which have recently been addressed in the spectroscopic study of Torres (2023).

This study is part of a series to incorporate current capabilities into studies of Cepheid masses.

1.1. *Polaris*:

Polaris (α UMi, HR 424, HD 8890, $V = 2.02$ mag) is the nearest and brightest classical Cepheid. It is a member of a triple system with a resolved 8th magnitude physical companion at a separation of 18". The Cepheid has been known for many years to be a single-lined spectroscopic binary with a period of about 30 years (Roemer 1965; Kamper 1996), with components designated Aa (the Cepheid) and Ab. A thorough compilation of radial velocity data has recently been produced by Torres (2023), resulting in a definitive orbit.

While Polaris Aa is a Cepheid, albeit with a small amplitude, it has several characteristics which are unusual.

- It pulsates in the first overtone (Feast and Catchpole 1997)
- It has an unusually rapid period change (Neilson et al. 2012). For fundamental mode pulsators, the period change agrees with expectations of evolution through the instability strip. For overtone pulsators, some additional factor seems to be involved (Evans et al. 2018).
- The pulsation amplitude can vary. Specifically, it decreased from about 1960 to 1990 (Arellano Ferro 1983). However, it did not die out completely (cease pulsation), but in about 2000 began to increase (e.g. Bruntt et al. 2008; Anderson 2019). Anderson, indeed, found the amplitude to be very stable over the course of 7 years.
- In addition, there was a “glitch” (phase jump) in the O-C period residuals about 1960 (Arellano Ferro 1983; Turner et al. 2005).
- The instability strip crossing in which Polaris is located has been extensively discussed. Based on the most recent distance and the sign of the period change, Evans et al. (2018) concluded it is on the third crossing, although it has been argued that it is on the first crossing (Anderson 2018).
- The possibility that the Cepheid itself may be the product of a merger is discussed by Bond et al. (2018), Evans et al. (2018) and Anderson (2018), based on the fact that the distant component Polaris B is too cool to match the isochrone of 100 Myr which fits the Cepheid, Polaris Aa.
- The single observation of Polaris to detect polarization (Barron et al. 2022) found much more complicated Stokes V profile than for other Cepheids implying a complex magnetic field. However, the profile is similar to the non-variable supergiant α Per (Grunhut et al. 2010), which perhaps reflects the very low pulsation amplitude.
- Several studies have searched for additional periodicities in the radial velocities (Lee et al. (2008) Anderson (2019), and other studies discussed therein). A periodicity of approximately 120 days was found by Lee et al., for instance, which they identify as due to rotation in a star with spots. Two periodicities (40.2 and 60 d) found by Anderson; 120d is an integral multiple of these.

These topics are fully discussed and references to all the velocity data sources are provided by Torres (2023). In this discussion these apparently exceptional properties are placed in the context of Cepheids. The times of periastron passage of Polaris coincide with the amplitude changes and also the phase jump at about 1960. In the extensive study of period changes in Cepheids, Csoranyi et al. (2022) find a number with phase jumps, as was found by Szabados previously (1991, 1989, and references therein). They are often found in short period overtone pulsators, and it was suggested by Szabados (1992) that they are likely to be found in binaries. This would link a number of the peculiarities related to Polaris to phenomena seen in other Cepheids, and provide a physical explanation. On one hand, this is surprising because the Polaris Aa and Ab system is comparatively wide. Torres estimates that the periastron separation between the two stars is 6.2 au, or approximately 29 times the Cepheid radius. On the other hand, the orbit is eccentric ($e = 0.635$), providing a variation of conditions around the orbit. The wide orbit would make it surprising for a characteristic such as a phase jump to be produced by simple tidal interaction. However, overtone pulsators are more erratic in their periods than fundamental mode pulsators, presumably for reasons we do not completely understand. Of course, these peculiarities may exist in other stars but have not been identified because they do not have such long and well covered datasets.

An important parameter in determining properties of Polaris is its distance. Specifically, the determination of the total mass in the system depends on the distance to convert the angular separation to au. The distance has been controversial, partly because of difficulties because Polaris is very bright. Recent distance determinations are summarized by Engle et al. (2018). Polaris B is the wide companion at a distance of $18''$ from the Polaris A system. It can be used for distance determination. Bond et al. (2018) argued that Polaris A and B form a gravitationally bound system, which allows us to use Polaris B for distance determination. The distance to Polaris B using *Gaia* DR3 (Gaia Collaboration et al. 2023) including the Lindegren parallax offset is 136.90 ± 0.34 pc (Gaia Collaboration et al. 2023; Lindegren et al. 2021). The distance will be reviewed when the *Gaia* DR4 is available, including corrections such as discussed in Khan et al. (2023).

Several previous steps have led up to the measurement of the mass of the Cepheid. The binary system discussed here is Polaris A made up of the Cepheid Polaris Aa and the companion Polaris Ab. Kamper (1996) published an orbit, (with additional velocities by Kamper and Fernie [1998]) In addition, Wielen et al. (2000) determined the inclination and the position angle of the line of nodes by comparing the proper motion from the *Hipparcos* satellite with the average long term ground-based proper motion. The final parameter to determine the mass was the separation of Aa and Ab. This system was resolved with *HST* (Evans et al. 2008) using the ACS camera. This provided the mass of the Cepheid of $4.5_{-1.4}^{+2.2} M_{\odot}$. This was followed up with three observations between 2007 and 2014 using the WFPC2 and WFC3 since the ACS HRC (high resolution channel) was no longer available (Evans et al. 2018). The astrometry from these observations was less accurate. However since they cover a quarter of the orbit, the inclination could be determined from them as well as the separation between the components. The present paper discusses observations around the orbit continued with CHARA and a speckle observation from Apache Point Observatory (APO).

The sections below contain the CHARA interferometric observations including data reduction and analysis, the diameter and surface imaging of Polaris, APO speckle observations, the orbit fitting, and discussion of the results.

2. INTERFEROMETRIC OBSERVATIONS AND DATA REDUCTION

We collected long-baseline optical interferometric data at Georgia State University’s Center for High Angular Resolution Astronomy (CHARA) Array (ten Brummelaar et al. 2005) located at Mount Wilson Observatory. The CHARA Array consists of six 1 m aperture telescopes in an Y-shaped configuration with two telescopes along each arm, oriented to the east (E1, E2), west (W1, W2) and south (S1, S2), offering good coverage of the (u, v) plane. The baselines range from 34 m to 331 m, providing an angular resolution down to 0.5 mas at $\lambda = 1.6 \mu\text{m}$. The data on Polaris were collected with the Michigan InfraRed Combiner (MIRC; Monnier et al. 2004) before 2017.5 and the upgraded Michigan InfraRed Combiner-eXeter (MIRC-X, Anugu et al. 2020) after 2017.5. MIRC and MIRC-X combine the light from all six telescopes simultaneously in the *H*-band, providing up to 15 fringe visibilities and 20 closure phase measurements across multiple spectral channels.

At the location of Polaris in the sky, we can combine only four telescopes at a time because of limitations on the length of the CHARA delay lines. Initially we used the low spectral resolution mode (prism $R = \lambda/\Delta\lambda = 50$) with MIRC and MIRC-X. Bandwidth smearing limits the effective field of view to ~ 50 mas (given by $\lambda^2/\Delta\lambda$) for the low spectral resolution mode. This resolution was sufficient to resolve the Ab companion during closest approach, however, detecting the companion became more challenging as the relative separation increased from orbital motion. In September 2019, we switched to higher spectral resolution modes (prism $R = 102$, grism $R = 190$) to extend the interferometric field of view to 100 mas and 190 mas, respectively. A log of our observations is available in Table 1.

Table 1. Log of the MIRC and MIRC-X observations at the CHARA Array.

UT Date	Combiner	Configuration	Mode	N_{sets}	N_{spec}	N_{vis}	N_{CP}	Calibrators
2016Sep12*	MIRC	W1E1E2W2	R=50	1	8	1472	976	1, 2
2016Nov18	MIRC	W1E1E2W2	R=50	1	8	1488	960	1, 2
2018Aug27	MIRC-X	W1E1E2W2	R=50	3	10	5560	3660	1, 3
		W1S2E1E2	R=50	3	10	5740	3780	1, 3
2019Apr09	MIRC-X	E1W2W1E2	R=50	4	6	3216	2016	1, 3
		E1W1S2E2	R=50	3	6	2310	1212	1, 3

Table 1 continued on next page

Table 1 (*continued*)

UT Date	Combiner	Configuration	Mode	N_{sets}	N_{spec}	N_{vis}	N_{CP}	Calibrators
2019Sep02*	MIRC-X	E1W2W1E2	R=102	1	13	1287	816	1, 2
		E1W2W1E2	R=190	2	31	6076	3870	1, 2
2021Apr02*	MIRC-X	E1W2W1E2	R=190	3	32	8256	5115	1, 3, 4
		E1W1S2E2	R=190	2	32	9664	6169	1, 3, 4
2021Apr03*	MIRC-X	E1W2W1E2	R=190	5	33	11187	5920	1, 3, 4
2021Apr04*	MIRC-X	E1W2W1E2	R=190	4	33	9174	4576	1, 3, 4
		E1W1S2E2	R=190	4	33	11649	7520	1, 3, 4

NOTE—The nights of 2018–2021 include two different telescope configurations and/or different spectral modes. The table gives the number of observing sets (N_{sets}) and the number of spectral channels (N_{spec}). It also lists the number of visibility (N_{vis}) and closure phase (N_{CP}) measurements for the reduction using the 30 second integration time. We adopted uniform disk diameters in the H -band for the calibrators from the JMMC angular diameter catalog (Bourgés et al. 2014): 1: HD 6319, $\theta_{\text{UDH}} = 0.740 \pm 0.078$ mas, 2: HD 12918, $\theta_{\text{UDH}} = 0.622 \pm 0.058$ mas, 3: HD 42855, $\theta_{\text{UDH}} = 0.758 \pm 0.078$ mas, and 4: HD 204149 $\theta_{\text{UDH}} = 0.671 \pm 0.065$ mas. An asterisk next to the UT date indicates nights where we detected the Ab companion.

Each observation consisted of recording 10 minutes of fringe data on Polaris followed by a shutter sequence to measure backgrounds, foregrounds, and the ratio of light between the fringe data and the photometric channels for each telescope. We monitored the interferometric transfer function by observing unresolved calibrator stars before and after each observation of Polaris. The calibrators were selected using the SearchCal software¹ (Bonneau et al. 2011) provided by the Jean-Marie Mariotti Center (JMMC). The calibrators and their adopted angular diameters (Bourgés et al. 2014) are listed in Table 1.

The data were reduced using the standard pipelines for MIRC (Monnier et al. 2007) and MIRC-X² (version 1.3.5; Anugu et al. 2020). The pipelines produce squared visibilities and triple products for each baseline and spectral channel. We used an integration time of 30 sec for improved detection of the faint companion located at separations that ranged from 30–85 mas. We also produced OIFITS files (see Section 3.2) that were averaged over each 10 min observing block for measuring the angular diameter and imaging the surface of Polaris Aa. We used a calibration script written in IDL by J.D. Monnier with the “deep cleaning” option to remove outliers. The reduced and calibrated OIFITS files will be available through the JMMC Optical Interferometry Database³ (OIDB) An example of data collected on UT 2019Sep02 are displayed in Figure 1.

¹ <http://www.jmmc.fr/searchcal>

² https://gitlab.chara.gsu.edu/lebouquj/mircx_pipeline.git

³ <https://www.jmmc.fr/english/tools/data-bases/oidb/>

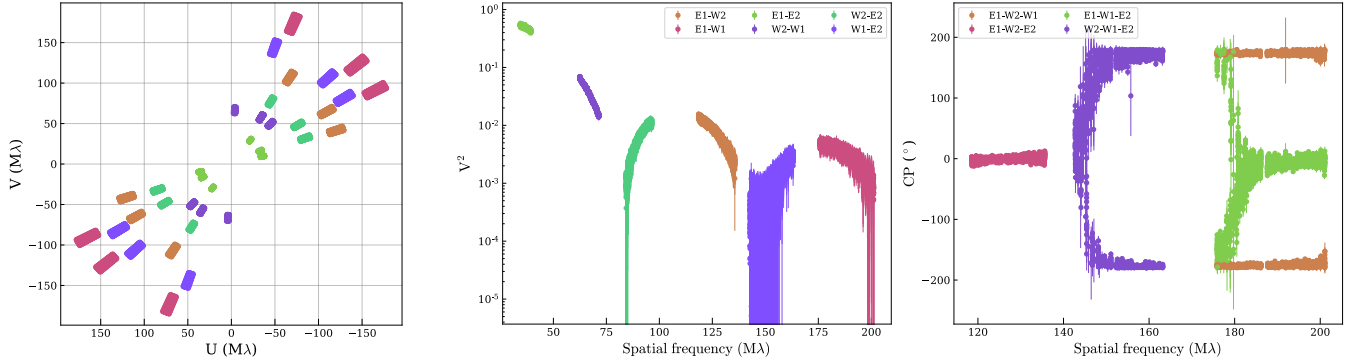


Figure 1. (u, v) coverage (left), squared visibilities (middle), and closure phase data (right) for the CHARA MIRC-X observations of Polaris on UT 2019Sep02. The closure phase data is plotted against the spatial frequency of the longest baseline in the closed triangle.

There were occasional offsets and more scatter than expected in some of the uncalibrated visibilities, particularly on the baselines including the E2 telescope in April 2021. These discrepancies showed up between different calibrators and sometimes within a data set on the same target. Figure 2 shows an example where the visibilities on E1-E2 baseline scatter upwards during the observation of calibrator HD 204149 and during the second set on Polaris. In both of these cases, the discrepant visibilities appeared after a brief pause in the data collection to realign the starlight into the MIRC-X fibers. We could not find a definitive cause for the discrepant observations; it could be related to vibrations in the E2 delay line cart while tracking at very slow speeds in the north or telescope oscillations while pointing at the pole. We inspected the visibility transfer functions from each night to reject measurements that were clearly discrepant.

The angular diameters and binary separations computed in Section 3 were multiplied by factors of 1.004 ± 0.0025 for MIRC and divided by 1.0054 ± 0.0006 for MIRC-X (J.D. Monnier, private communication). This is equivalent to adjusting the respective wavelengths reported in the OIFITS files by the same factors.

3. DATA ANALYSIS

3.1. Diameter Measurements of Polaris Aa

We began our analysis of the interferometric data by fitting the squared visibility amplitudes for the angular diameter of Polaris Aa. The limb-darkening was parameterized with the linear function $I_\lambda(\mu) = I_\lambda(1)[1 - u_\lambda(1 - \mu)]$ (Hanbury-Brown et al. 1974), with $\mu = \cos \zeta$, where ζ is the angle between the line of sight and a surface element of the star. We solved for the limb-darkened diameter (θ_{LD}), limb-darkening coefficient (u_λ), and visibility scaling factor (V_0) to account for visibility miscalibrations or the presence of extended flux. The squared visibilities of the limb-darkened model are multiplied by V_0 before comparing with the measured values. We first performed a grid search through the three parameters to find the best fit and then followed a Monte Carlo bootstrap approach with 1000 iterations to determine uncertainties. For each bootstrap iteration, we randomly selected measurements with repetition to construct a new set of visibilities with some measurements repeated and some left out. We then applied Gaussian uncertainties to the resampled measurements and fit a limb-darkened model using the IDL MPFIT package (Markwardt 2009) to optimize the fit for each iteration. We adopted the standard deviation of the bootstrap distributions as the uncertainties on each parameter. The angular diameters had been corrected using the wavelength calibration factors discussed in Section 2. To minimize scatter in the observations, the angular diameters were fit to the squared visibilities averaged over the 10-minute observing sets. The results from the diameter fits are presented in Table 2.

We measured a mean diameter of $\theta_{LD} = 3.143 \pm 0.027$ mas and a mean limb-darkening coefficient of $u_\lambda = 0.120 \pm 0.043$. At the *Gaia* distance of 136.90 ± 0.34 pc this corresponds to a mean radius of $46.27 \pm 0.42 R_\odot$. On most nights, the scaling factor V_0 was greater than 1.0, indicating that the V^2 measurements are higher than the limb-darkened model. This implies a “negative” background flux, indicating that the scaling term likely arises because of a miscalibration of the visibilities, rather than a physical cause like extended flux outside the field of view. The calibration issues discussed in Section 2, as well as uncertainties in the partially resolved calibrator diameters, could have contributed to the miscalibration. The mean diameter is consistent within the uncertainties with the interferometric diameter measured with the FLUOR instrument at the CHARA Array (Mérand et al. 2006). However, the calibration of the MIRC/MIRC-X visibilities was not accurate enough to confirm the presence of the extended circumstellar envelop

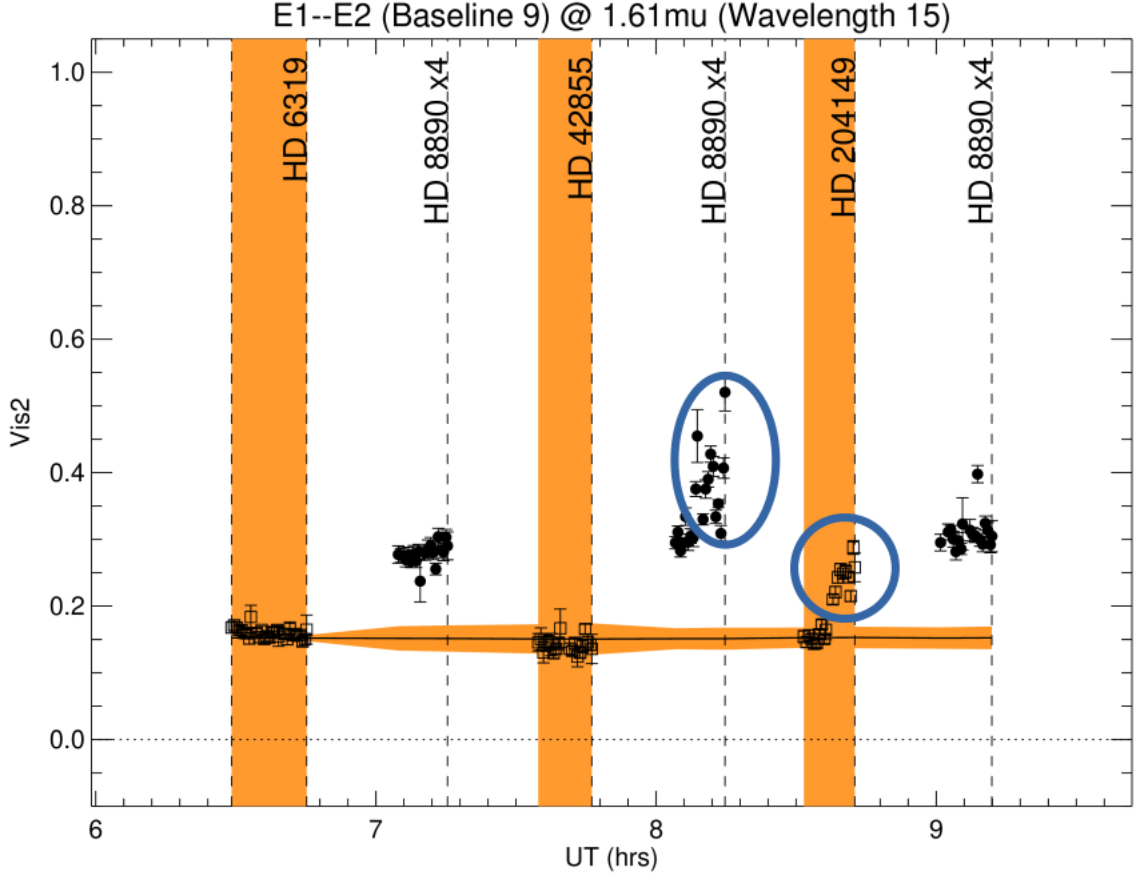


Figure 2. Visibility transfer function for the E1-E2 baseline on UT 2021 Apr 02 for the E1E2W1W2 configuration. The calibrators are marked by the orange shaded regions. The visibilities of Polaris have been multiplied by a factor of four to make them more visible on the plot. Circled in blue are two regions showing discrepant visibilities on Polaris and calibrator HD 204149.

reported by [Mérand et al. \(2006\)](#).

To investigate whether we see changes in the diameter over the 4-day pulsation cycle, we fit the diameters separately for each configuration observed on each night as shown in Table 2. We adopted the ephemeris of [Berdnikov & Pastukhova \(1995\)](#) for the times of maximum light:

$$\text{HJD}_{\text{max}} = 2,428,260.727 + 3.969251E \quad (1)$$

To account for the changing pulsation period, we used the O-C diagram in Figure 6 of [Torres \(2023\)](#) to calculate the times of maximum light nearest to each angular diameter measurement. The columns in Table 2 are the date of the observation, the HJD -2,400,000, the time of maximum light used to compute the phase, the angular diameter and the limb darkening coefficient, the scaling factor, the angular diameter from a fixed limb darkening coefficient $u_{\lambda} = 0.120$, and the number of visibility measurements. We plot the limb-darkened diameters with the fixed limb darkening coefficient against the pulsation phase in Figure 3. The dashed line represents the mean angular diameter and the dotted lines show 0.4% variation in diameter expected from pulsation ([Moskalik & Gorynya 2005](#)). The standard deviation of the mean diameter is 2.1 times larger than the variation expected from pulsation. Cepheids are expected to reach a minimum **angular diameter** around phase 0.8, which is roughly consistent with our measurements. However, the variations in the measured diameters could also be impacted by the visibility miscalibrations discussed in Section 2.

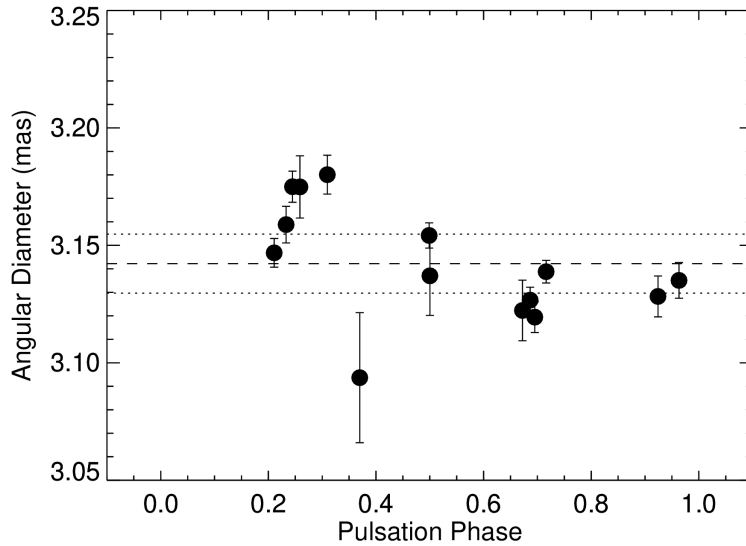


Figure 3. Limb-darkened diameters of Polaris Aa plotted against the pulsation phase. The dashed line represents the mean angular diameter and the dotted lines show 0.4% variation in diameter expected from pulsation (Moskalik & Gorynya 2005).

Table 2. Limb-darkened diameter fits for Polaris Aa.

UT Date	HJD	T_{max}	θ_{LD} (mas)	u_{λ}	V_0	θ_{fxu} (mas)	N_{vis}
2016Sep12	57643.736	57641.7504	3.1257 ± 0.0169	0.083 ± 0.044	1.2089 ± 0.0298	3.1370 ± 0.0169	96
2016Nov18	57710.744	57709.2759	3.1042 ± 0.0277	0.156 ± 0.064	0.8628 ± 0.0501	3.0937 ± 0.0277	96
2018Aug27	58357.744	58356.7171	3.1769 ± 0.0133	0.127 ± 0.037	1.2848 ± 0.0350	3.1749 ± 0.0133	360
2018Aug27	58357.946	58356.7171	3.1811 ± 0.0083	0.125 ± 0.033	1.2695 ± 0.0296	3.1801 ± 0.0083	360
2019Apr09	58582.815	58579.1471	3.1278 ± 0.0087	0.119 ± 0.024	1.2352 ± 0.0145	3.1283 ± 0.0087	216
2019Apr09	58582.970	58579.1471	3.1386 ± 0.0076	0.136 ± 0.023	1.3896 ± 0.0184	3.1351 ± 0.0076	180
2019Sep02	58728.777	58726.1087	3.1095 ± 0.0129	0.074 ± 0.038	1.0904 ± 0.0182	3.1223 ± 0.0129	78
2019Sep02	58728.868	58726.1087	3.1392 ± 0.0065	0.186 ± 0.018	1.1135 ± 0.0079	3.1194 ± 0.0065	372
2021Apr02	59306.839	59306.0020	3.1377 ± 0.0061	0.089 ± 0.018	0.9053 ± 0.0066	3.1468 ± 0.0061	576
2021Apr02	59306.927	59306.0020	3.1484 ± 0.0078	0.065 ± 0.025	1.0072 ± 0.0108	3.1588 ± 0.0078	192
2021Apr02	59306.974	59306.0020	3.1848 ± 0.0066	0.167 ± 0.018	0.8198 ± 0.0064	3.1750 ± 0.0066	384
2021Apr03	59307.982	59306.0020	3.1747 ± 0.0054	0.189 ± 0.014	1.1104 ± 0.0090	3.1542 ± 0.0054	660
2021Apr04	59308.727	59306.0020	3.1179 ± 0.0055	0.089 ± 0.015	1.1564 ± 0.0111	3.1267 ± 0.0055	594
2021Apr04	59308.845	59306.0020	3.1289 ± 0.0048	0.069 ± 0.016	1.0364 ± 0.0088	3.1388 ± 0.0048	792

3.2. Surface Imaging of Polaris Aa

The limb-darkened diameter model does a reasonable job fitting the squared visibility amplitudes. However, the strong non-zero and non-180° closure phases (see Figure 1) suggest the presence of asymmetries on the surface of Polaris Aa. Initial modeling of the data indicated that these strong deviations in the closure phases are not produced by the faint binary companion Ab. Modeling with PMOIRE⁴ (Mérand 2022) and a custom-made routine in IDL, indicates that a few starspots on the surface of Polaris Aa can account for most of the closure phase signal. However, the size, location, and contrast of the spots are not well-constrained due to the limited (u, v) coverage during the

⁴ <https://github.com/amerand/PMOIRE>

observations.

We also reconstructed images of the stellar surface of Polaris Aa using SQUEEZE⁵ (Baron et al. 2010, 2012), SURFING (e.g., Roettenbacher et al. 2016), and ROTIR⁶ (Baron 2020). Both SURFING and ROTIR perform the image reconstructions on the surface of a spheroid, constraining the size and shape of the star which is important given the limited (u, v) coverage of the observations. ROTIR is written in Julia and uses the OITools libraries⁷, a package for visualizing, modeling, and imaging interferometric data. We used the total variation regularizer with a weight of 0.01-0.05 for ROTIR. To prepare the OIFITS files for imaging, we corrected the visibilities for each individual data set using V_0 scaling factors computed from limb-darkened diameter fits; we used the data averaged over the 10-minute observing sets. We merged together the datasets from all configurations on a given night to improve the (u, v) coverage for the image reconstructions. For the data from April 2021, we merged the data together from the three consecutive nights.

Figure 4 shows the image of Polaris Aa reconstructed with SURFING and ROTIR for the epoch with the most complete (u, v) coverage from UT 2021 Apr 2, 3, and 4. Both images show a large bright spot to the north of center. We show the SURFING and ROTIR images from four different nights and the corresponding (u, v) coverage in Figure 5. All of the images show spots on the surface, however, some of the surface features could be created by artifacts in the reconstruction process due to gaps in the (u, v) coverage or systematic errors in the visibility calibration. The bottom row in Figure 5 shows reconstructed images from simulated data of a simple limb-darkened model without spots and with the same (u, v) sampling of Polaris to show which features are likely to be artifacts and which are likely to be spots on the surface. The contrast of the surface spots in the real data is larger than the contrast in the simulated limb-darkened disk data. In addition to having much lower contrast, the spots in the simulated data are distributed in point symmetric patterns around the center of the star. The spots in the real data that do not follow these point-symmetric patterns are more likely to be true features on the stellar surface. Changing the simulated noise in the limb-darkened models changes slightly the shape and orientation of the artifacts in the simulated images, however the large-scale structure of the patterns remain consistent between iterations with different simulated noise. The mirroring of bright and dark spots about the origin during some of the Polaris epochs is likely an artifact of the reconstruction process, however these features are indicative of an asymmetry in brightness distribution. The interferometric data and observables extracted from the reconstructed images are shown in Appendix A.

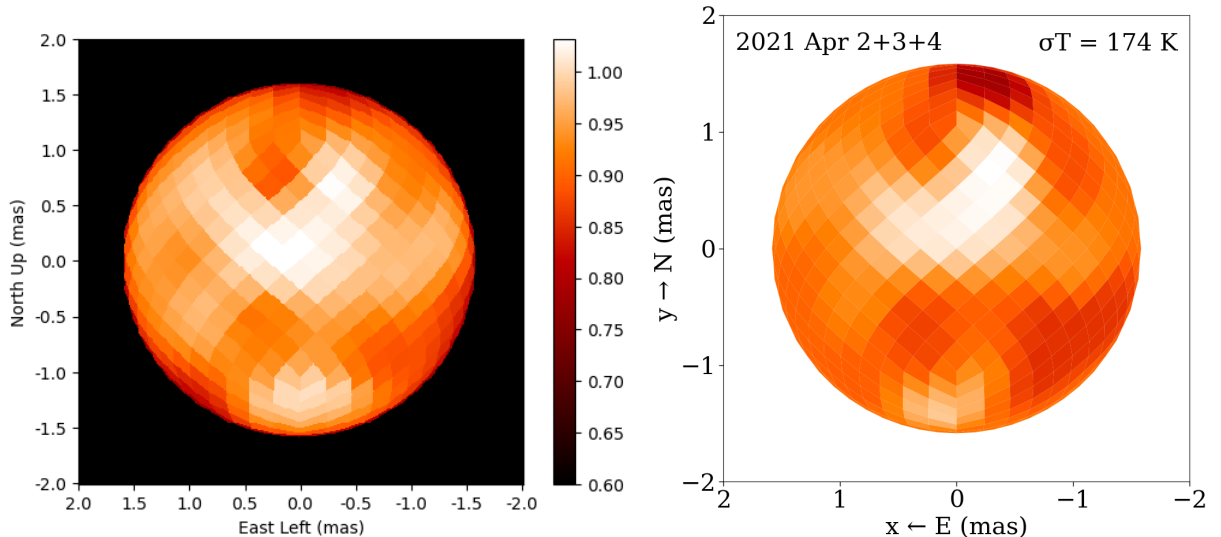


Figure 4. Surface images of Polaris Aa reconstructed using SURFING (left) and ROTIR (right) on the merged data set from UT 2021Apr02, 2021Apr03, and 2021Apr04.

3.3. Binary Positions of Polaris Aa,Ab

⁵ <https://github.com/fabienbaron/squeeze>

⁶ <https://github.com/fabienbaron/ROTIR.jl>

⁷ <https://github.com/fabienbaron/OITools.jl>

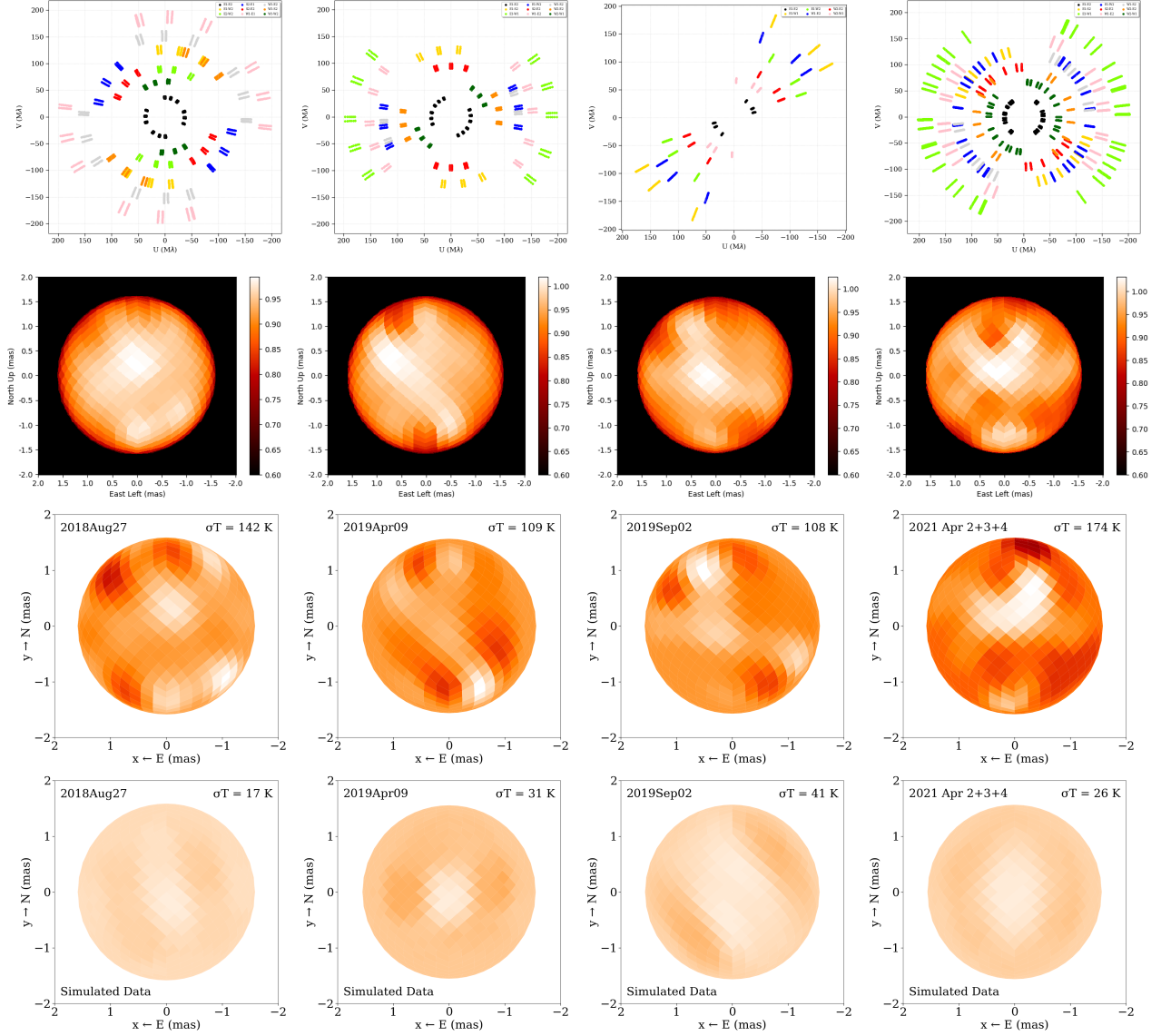


Figure 5. Surface images of Polaris Aa reconstructed from the CHARA data on four different nights. The top row shows the (u, v) coverage, the second row shows the Polaris images reconstructed using SURFING, the third row shows images reconstructed using ROTIR, and the bottom row shows images reconstructed from simulated data of a limb-darkened disk model without spots and with the same (u, v) sampling as the Polaris data. The simulated data highlights artifacts in the reconstruction from gaps in the (u, v) coverage. For the ROTIR images, the standard deviation in the surface temperature is listed in the upper right of each panel.

We used the data sets with 30-second integration times to search for the faint companion (Polaris Ab). The shorter integration time reduces time-smearing of the companion signal given the separations of 40–85 mas expected from the previous orbit fit. To account for the asymmetries on the surface of Polaris Aa, we first reconstructed images with SQUEEZE using all of the data from a given night. We then used a modified version of the IDL Binary Grid Search Procedure⁸ (Schaefer et al. 2016) where we extract visibilities and closure phases directly from the reconstructed image of Polaris Aa and analytically add in the companion. We started the grid search at the expected location of the binary based on the orbit computed by Evans et al. (2018) and searched within $\Delta\text{RA} = \pm 20$ mas and $\Delta\text{DEC} = \pm 20$ mas from the initial values. We applied a correction for bandwidth smearing to the binary fit. The results from the binary grid search are shown in supplementary files.

⁸ <http://www.chara.gsu.edu/analysis-software/binary-grid-search>

We detected the Ab companion on five nights; these nights are indicated by an asterisk next to the UT date in Table 1. On the nights with non-detections, the data quality was poor (e.g., 2016-11-18) or Polaris Ab was located outside of the interferometric field of view given by $\lambda^2/\Delta\lambda$. The field of view corresponds to 50 mas in the low spectral resolution mode of MIRC and MIRC-X, so with an expected separation of ~ 70 mas, we suspect that bandwidth smearing compromised the binary signal on UT 2018Aug27 and 2019Apr09. We were able to recover the detection of the companion on subsequent dates when we used the higher spectral resolution Prism102 and Grism190 modes with a field of view of 100 and 190 mas, respectively.

The average contrast of the companion was $\Delta H = 7.8 \pm 0.4$ mag, beyond the typical detection limits of the MIRC and MIRC-X instruments (Gallenne et al. 2015). To improve our confidence in the solutions, we also performed the binary grid search separately for each configuration observed on a given night. For the nights with high confidence solutions, the separations measured from each configuration separately were consistent with the results based on the full night of data. Additionally, the three successive nights in April 2021 produced consistent binary solutions.

We used a bootstrap approach with 100 iterations to estimate the uncertainties based on the 67.5% confidence ellipses for two parameters from the bootstrap distributions. These errors are added in quadrature with the uncertainties from the wavelength calibration. The best fit binary positions (corrected for wavelength calibration) and flux ratios (f_{Ab}/f_{Aa}) are listed in Table 3. The positions of Polaris Ab relative to Aa are given as the separation (ρ) and position angle measured east of north (PA). We also list the separations projected into right ascension ($\Delta\alpha$) and declination ($\Delta\delta$). The error ellipses are given by the semi-major axis (σ_{maj}), semi-minor axis (σ_{min}), and the position angle of the major axis (σ_{PA}). The dates are given as heliocentric Julian day (HJD) and Julian year (JY). In Table 3, we also collected the *HST* astrometric measurements reported by Evans et al. (2008, 2018) in both polar and Cartesian coordinates. These papers reported the dates in Besselian years which we have converted to JY.

3.3.1. Confirmation of binary positions with CANDID

We confirmed the companion detections using the *CANDID* tool⁹ (Companion Analysis and Non-Detection in Interferometric Data, Gallenne et al. 2015). *CANDID* is a set of Python tools allowing us to search systematically for companions and estimate detection limits using all interferometric observables. We used the implemented bootstrap function to estimate the uncertainties on our previous parameters. In *CANDID*, limb-darkening is parameterized with a power law function $I_\lambda(\mu) = I_\lambda(1)\mu^\epsilon$, and we chose to fix this parameter to 0.15. Bootstrapping is performed on the MJDs with our previous fitted parameters and using 1000 bootstrap samples. From the distribution, we took the median value and the maximum value between the 16th and 84th percentiles as uncertainty for the flux ratio and angular diameter. For the fitted astrometric position, the error ellipse is derived from the bootstrap sample (using a principal components analysis). The positions and uncertainties measured with *CANDID* were consistent with those determined from the IDL grid search procedure.

Table 3. Relative astrometric position of the Polaris Ab companion..

HJD –	JY	ρ	PA	$\Delta\alpha$	$\Delta\delta$	σ_{maj}	σ_{min}	σ_{PA}	f_{Ab}/f_{Aa}
2,400,000		(mas)	($^\circ$)	(mas)	(mas)	(mas)	(mas)	($^\circ$)	
<i>CHARA</i>									
57643.735	2016.6974	33.008	71.696	31.338	10.366	5.757	1.159	18.49	0.00089 ± 0.05838
58728.831	2019.6683	75.537	340.239	-25.538	71.088	0.833	0.547	40.73	0.00072 ± 0.00744
59306.890	2021.2509	84.507	315.900	-58.810	60.686	1.200	0.663	94.49	0.00110 ± 0.00789
59307.982	2021.2539	84.447	315.787	-58.888	60.527	10.736	3.954	123.45	0.00070 ± 0.02214
59308.785	2021.2561	84.232	315.669	-58.861	60.252	0.880	0.804	135.12	0.00045 ± 0.00363
<i>Speckle</i>									
60237.913	2023.800	98.8	286.7	-94.6	28.4	5.3	4.2	0.0	
<i>HST</i>									

Table 3 continued on next page

⁹ Available at <https://github.com/amerand/CANDID> or <https://github.com/agallenne/GUICandid>

Table 3 (*continued*)

HJD – 2,400,000	JY	ρ (mas)	PA ($^{\circ}$)	$\Delta\alpha$ (mas)	$\Delta\delta$ (mas)	σ_{maj} (mas)	σ_{min} (mas)	σ_{PA} ($^{\circ}$)	$f_{\text{Ab}}/f_{\text{Aa}}$
53585.488	2005.5866	172.4	231.407	-134.75	-107.54	2.1	2.1	0.0	
53961.416	2006.6158	169.6	226.385	-122.79	-116.99	3.1	3.1	0.0	
54298.514	2007.5387	180.0	223.000	-122.76	-131.64	20.0	20.0	0.0	
55153.597	2009.8798	150.0	216.000	-88.17	-121.35	20.0	20.0	0.0	
56835.302	2014.4841	85.0	175.000	7.41	-84.68	20.0	20.0	0.0	

NOTE—Positions in Table 3 are for J2000.

4. SPECKLE OBSERVATIONS OF POLARIS

Polaris was observed using the technique of speckle interferometry at the Astrophysical Research Consortium (ARC) 3.5-m telescope at Apache Point Observatory (APO) on 2023 Oct 19 and 20. The speckle camera used was the Differential Speckle Survey Instrument (DSSI, Horch et al. 2009), which is currently a visitor instrument at APO. DSSI takes speckle patterns in two filters simultaneously; for the Polaris observations, we used filters with center wavelengths of 692 nm and 880 nm, and with FWHMs of 40 and 50 nm respectively. On each night, a total of nine thousand short-exposure images were recorded in each filter and stored in nine FITS files, each of which consisted of a 1000-frame stack of 256x256-pixel frames. The exposure time of individual frames was 40 ms, and the seeing was approximately 0.9 arcseconds on both nights.

The reduction and calibration of DSSI speckle data at APO is described in Davidson et al. (2024); briefly, we bias-subtract and form the spatial frequency power spectrum of individual frames, co-adding these in the Fourier domain to arrive at a summed power spectrum for each data file. We then deconvolve by dividing by the power spectrum of a bright point source observed in the same way. The result for a binary star is a pure fringe pattern, which we then fit using a downhill simplex algorithm as described in Horch et al (1997). The fringe spacing, orientation, and depth of the fringe minima determine the separation, position angle, and magnitude difference of the pair. In this analysis, we do not determine the quadrant of the secondary star; there is a 180-degree ambiguity in the position angle due to the fact that the power spectrum has no phase information. For the 2023 October speckle run at APO, the pixel scale and orientation were obtained using a combination of several binaries with extremely well-determined orbits and slit mask observations, as described in Davidson et al. (2024). These methods resulted in a pixel scale with uncertainty of approximately 0.24% and offset angles between pixel axes and celestial coordinates that are uncertain at the 0.1-degree level.

Polaris presents a complication in the speckle analysis because it is a system with a large magnitude difference that is observed at airmass of near 2.0 from Apache Point. The airmass adds dispersion to the speckle patterns, stretching speckles out on the image plane in a direction leading toward the zenith. This then changes the shape of the power spectrum and could affect the fringe fitting results. To have a good estimate of the speckle transfer function for a particular DSSI observation, a bright unresolved star is typically observed near in time and close in sky position to the star of interest. In the case of Polaris, since it was not possible to have as close a match in sky position as we typically use, we instead observed a bright unresolved star at low airmass, and then applied a dispersion model to that observation so that it matched Polaris' zenith angle and azimuth exactly. This removed most of the effect of the dispersion, but a further correction was applied by allowing for additional free parameters in the fringe fit to account for any residual dispersion in the Fourier domain. In this way, it was possible to determine relatively consistent relative astrometry and photometry of the system for the sub-sample of the files analyzed that had the lowest reduced-chi squared values from the fringe fitting procedure.

The measurements from the best sequences in the two nights of data resulted in the following average relative position: $\Delta\alpha = -0''.0902 \pm 0''.0053$ and $\Delta\delta = +0''.0404 \pm 0''.0042$, for the equinox of the date of observation (Julian year 2023.7999). These correspond to polar coordinates $\theta = 294^{\circ}1 \pm 3^{\circ}7$ and $\rho = 0''.0988 \pm 0''.0052$. Because of the dispersion complication noted above, we were not able to derive a reliable measure of the magnitude difference between Polaris and its companion.

Given that the rest of the astrometric measurements in this work are effectively referred to the equinox J2000, we applied rigorous precession to our result above in order to reduce it to that same frame of reference. The position angle correction is -7.4 . We obtained $\Delta\alpha = -0''.0946 \pm 0''.0053$ and $\Delta\delta = +0''.0284 \pm 0''.0042$ (J2000).

5. ORBIT FITTING

5.1. Radial Velocities

The orbital analysis depends on the combination of two datasets, the radial velocities and relative astrometry. The radial velocity dataset is very large and made up of measurements from many sources to cover multiple cycles of the 30 year orbit of Polaris Aa-Ab. We used the complete set of 3,659 radial velocities with pulsation removed that are tabulated in Table 3 of Torres (2023)¹⁰. To those we added an additional 16 Hermes velocities from the program VELOCE I (Anderson, et al 2024 in press). The data had been prepared using the template approach detailed in Anderson (2019). Initially we applied the radial velocity jitter and offset terms in Table 5 of Torres (2023) and the additional Hermes data. (Jitter is as defined in Torres [2023], the uncertainty for each dataset from the orbit fitting.) After experimentation and preliminary fits, the offsets and jitter were redetermined as listed in Table 4. The sources and references are as listed in Table 5 of Torres (2023). Successive pairs of columns to the right provide the radial velocity offset and jitter for the original orbit in Torres (2023), and the solution for radial velocities and CHARA and HST astrometry here.

Table 4. Corrections to Radial Velocity Sources

Source	Torres 2023		RV + Astrom	
	Offset km s ⁻¹	Jitter km s ⁻¹	Offset km s ⁻¹	Jitter km s ⁻¹
1 Roemer 1965	-	0.681	-	0.680
2 Hartmann 1901	+1.39	0.51	+1.43	0.52
3 Kustner 1908	+1.05	0.75	+0.94	0.83
4 Arellano Ferro 1983a + Kamper 1996	+1.027	0.524	+1.001	0.580
5 Dinshaw et al. 1989	-11.829	0.469	-11.694	0.450
6 Gorynya et al. 1992	+1.488	0.500	+1.375	0.498
7 Hatzes & Cochran 2000	-14.117	0.027	-14.242	0.027
8 Usenko et al. 2015	+0.068	0.387	+0.100	0.409
9 Kamper & Fernie 1998	-0.222	0.1061	-0.323	0.1065
10 Eaton 2020	+1.120	0.0444	+1.156	0.0398
11 Lee et al. 2008	-17.794	0.1103	-17.772	0.1124
12 Bucke 2021	-18.387	0.0976	-18.387	0.150
13 Anderson 2019	+0.551	0.0977	+0.622	0.1125
14 Anderson 2024	-	-	+0.440	0.103

5.2. Orbit

The astrometry dataset has only 11 two-dimensional data points that cover only 16 years, or half the orbit.

Table 5 lists the orbital parameters from the spectroscopic radial velocity orbit computed by Torres (2023) and Anderson et al. (2024) and a fit to only the visual orbit computed through a Newton Raphson technique using the IDL orbit fitting library¹¹ described by Schaefer et al. (2016). The orbital parameters include the orbital period P_{orb} ,

¹⁰ An error in the identification of some of the datasets in the online version of Table 3 of Torres (2023) was identified and corrected here

¹¹ <http://www.chara.gsu.edu/analysis-software/orbfit-lib>

time of periastron passage T_p , eccentricity e , argument of periastron with reference to the primary ω , primary radial velocity amplitude K_1 , systemic velocity γ , longitude of ascending node Ω for J2000, inclination i , and angular semi-major axis a . The eccentricity and ω_{Aa} differ by 1.4σ and 2.3σ , respectively, between the spectroscopic and visual orbits.

Our methods for fitting the radial velocities and astrometry simultaneously are described in the subsections below. It was realized early on that the analysis approach is particularly important since the orbit has a substantial eccentricity. In a preliminary solution weighted solely by the errors on the datapoints in the two datasets, the *HST* astrometry was systematically offset from the orbit. The eccentricity and ω_{Aa} are set essentially by the large number of radial velocities. We explored several approaches to combine the different datasets. The various weighting methods are described in more detail below with the orbital parameters from each solution listed in Table 5.

5.3. Weights based on Measurement Errors

To determine the orbital parameters, we simultaneously fitted the radial velocities (RVs) and astrometric position using a Markov chain Monte Carlo (MCMC) routine¹², whose log-likelihood function is given as (Gallenne et al. 2019a)

$$\log(\mathcal{L}) = -\frac{1}{2}\chi^2, \text{ with } \chi^2 = \chi_{\text{RV}}^2 + \chi_{\text{ast}}^2.$$

In our previous works on binary Cepheid systems with astrometric data (see e.g. Gallenne et al. 2019b; Gallenne et al 2018), both the pulsation and orbital motions of the Cepheids were fitted together with the astrometry. In this work, we decided to ignore the pulsation motion of the Cepheid by directly fitting the pulsation-corrected RVs from Torres (2023). In this case, our RV model is simply defined as

$$\chi_{\text{RV}}^2 = \sum \frac{(V_1 - V_{1\text{m}})^2}{\sigma_{V_1}^2},$$

in which V_1 and σ_1 denote the measured radial velocity and uncertainties for Polaris, and $V_{1\text{m}}$ is the Keplerian velocity model characterized by Heintz (1978):

$$\begin{aligned} V_{1\text{m}} &= \gamma + K_1 [\cos(\omega + \nu) + e \cos \omega], \\ \tan \frac{\nu}{2} &= \sqrt{\frac{1+e}{1-e}} \tan \frac{E}{2}, \\ E - e \sin E &= \frac{2\pi(t - T_p)}{P_{\text{orb}}}, \end{aligned}$$

where γ is the systemic velocity, e the eccentricity, ω the argument of periastron, ν the true anomaly, E the eccentric anomaly, t the observing date, P_{orb} the orbital period, T_p the time of periastron passage, and K_1 the primary radial velocity amplitude.

χ_{ast}^2 measure for astrometry depends on the astrometric measurements as

$$\begin{aligned} \chi_{\text{ast}}^2 &= \chi_{\text{a}}^2 + \chi_{\text{b}}^2, \\ \chi_{\text{a}}^2 &= \sum \frac{[(\Delta\alpha - \Delta\alpha_{\text{m}}) \sin \sigma_{\text{PA}} + (\Delta\delta - \Delta\delta_{\text{m}}) \cos \sigma_{\text{PA}}]^2}{\sigma_{\text{maj}}^2}, \\ \chi_{\text{b}}^2 &= \sum \frac{[-(\Delta\alpha - \Delta\alpha_{\text{m}}) \cos \sigma_{\text{PA}} + (\Delta\delta - \Delta\delta_{\text{m}}) \sin \sigma_{\text{PA}}]^2}{\sigma_{\text{min}}^2}, \end{aligned}$$

in which $(\Delta\alpha, \Delta\delta, \sigma_{\text{PA}}, \sigma_{\text{maj}}, \sigma_{\text{min}})$ denote the relative astrometric measurements with the corresponding error ellipses, and $(\Delta\alpha_{\text{m}}, \Delta\delta_{\text{m}})$ represent the astrometric model defined as:

$$\begin{aligned} \Delta\alpha_{\text{m}} &= r [\sin \Omega \cos(\omega + \nu) + \cos i \cos \Omega \sin(\omega + \nu)], \\ \Delta\delta_{\text{m}} &= r [\cos \Omega \cos(\omega + \nu) - \cos i \sin \Omega \sin(\omega + \nu)], \\ r &= \frac{a(1 - e^2)}{1 + e \cos \nu}, \end{aligned}$$

¹² With the Python package *emcee* developed by Foreman-Mackey et al. (2013).

where Ω is the longitude of ascending node, i the orbital inclination, and a the angular semi-major axis.

As a starting point for our 100 MCMC walkers, we performed a least squares fit using orbital values from [Torres \(2023\)](#) as first guesses. We then ran 100 initialization steps to well explore the parameter space and get settled into a stationary distribution. For all cases, the chain converged before 50 steps. Finally, we used the last position of the walkers to generate our full production run of 1000 steps, discarding the initial 50 steps. All the orbital elements are estimated from the distribution taking the median value and the maximum value between the 16th and 84th percentiles as uncertainty (although the distributions were roughly symmetrical).

Polaris is a single-lined spectroscopic binary which does not allow the individual masses to be determined independently without additional information. To this end we adopt the *Gaia* distance for Polaris B (above). In our MCMC procedure, we included the parallax measurement using a normal distribution centered on 7.3045 mas with a standard deviation of 0.0178 mas. Masses are then derived with the following equations:

$$\begin{aligned} M_T &= \frac{a^3}{P_{\text{orb}}^2 \varpi^3}, \\ M_2 &= \frac{0.03357 a^2 K_1 \sqrt{1 - e^2}}{\varpi^2 P_{\text{orb}} \sin i} \\ M_1 &= M_T - M_2 \end{aligned}$$

with $M_T = M_1 + M_2$ the total mass in M_\odot , a and ϖ in mas, P_{orb} in years, and K_1 in km s^{-1} .

Initially, when fitting the orbit simultaneously to the radial velocities and astrometry, we weighted each measurement by their respective uncertainties. We performed a similar fit weighted by measurement uncertainties using the IDL orbit fitting library, but with uncertainties computed through a bootstrap technique. The orbital parameters from this fit are listed in the “ σ Weights” Column of Table 5.

5.4. Weights based on $N\sigma$

To more evenly weight the two datasets, we can compute an average χ^2 statistic multiplying the χ^2 from each dataset by $1/N$, where N is the number of data points ([Mérand et al. 2015](#), equation 5). The total χ^2 for the simultaneous fit then becomes:

$$\chi^2 = \frac{1}{N_{\text{RV}}} \chi_{\text{RV}}^2 + \frac{1}{N_{\text{ast}}} \chi_{\text{ast}}^2.$$

where N_{RV} is the number of radial velocity measurements and N_{ast} is the number of astrometry data points. The orbital parameters are listed in the “ $N\sigma$ Weight” Column of Table 5. Uncertainties in the orbital parameters were determined from MCMC distributions.

5.5. Replicating the Astrometric Measurements

Another weighting scheme is motivated by the Synthetic Minority Over-sampling Technique (SMOTE) used in the machine learning community ([Chawla et al. 2002](#)). In order to weight the two sets of measurements more evenly, we replicated each position measurement 167 times to give roughly even number of observables ($N = 167 \times 11 \times 2 = 3674$). We applied random Gaussian uncertainties to the replicated measurements, creating a swarm of simulated observables for each data point. We then fit a simultaneous orbit to the radial velocities and the replicated positions using the IDL orbit fitting library¹³. We followed a Monte Carlo bootstrap approach to compute uncertainties. For each bootstrap iteration, we randomly selected from the 11 astrometric measurements, with repetition. We then applied Gaussian uncertainties to the resampled measurements and replicated each data point as described above. We repeated this process 1,000 times and computed uncertainties in the orbital parameters from the standard deviation of the bootstrap distributions. The orbital parameters from this fit are listed in the “Replicated” column of Table 5. The spectroscopic and astrometric orbits are shown in Figure 6. The orbital parameters and uncertainties are consistent with the $1/N$ weighting method. The averaged χ^2 in Section 5.4 under-weights the radial velocities, while the replicated points over-weight the astrometry; but both methods provide similar results in the end.

In summary, all three weighting schemes produced similar masses within the errors. As stated in Section 5.2 the solution based on measurement errors (Section 5.3) the astrometric points from *HST* ACS/HRC are systematically displaced from the orbit solution. Thus, the astrometry is poorly represented. This is possibly due to systematic errors

¹³ <http://www.chara.gsu.edu/analysis-software/orbfit-lib>

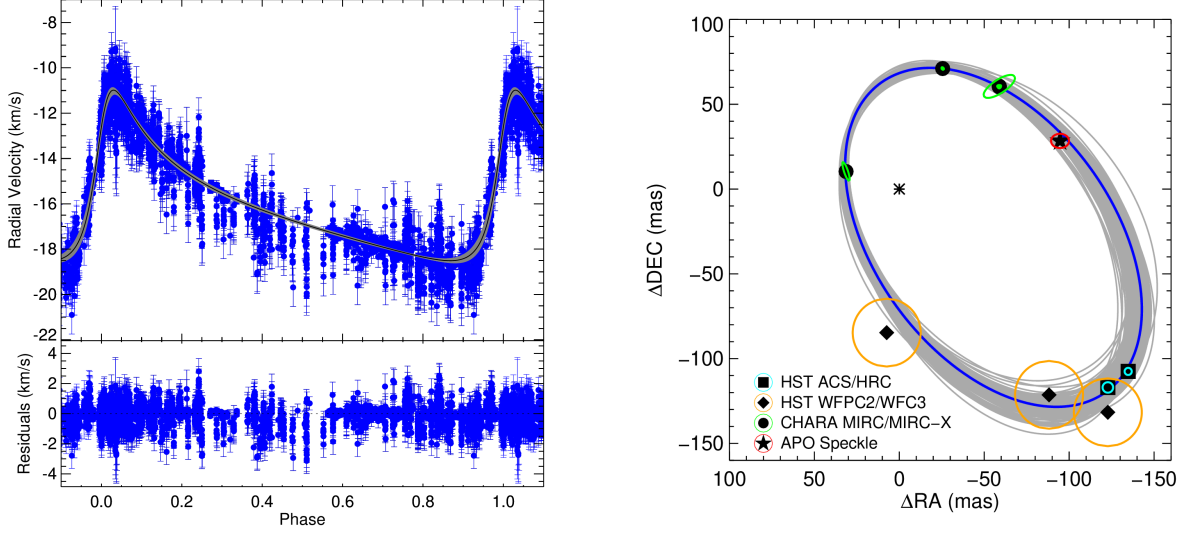


Figure 6. Spectroscopic (left) and astrometric (right) orbital fit of Polaris. The symbols for the measurements by *HST* ACS, the *HST* WFPC2 and WFC3, CHARA, and APS speckle are shown in the figure. In addition to the best fit orbit, overplotted in gray is a sample of 1000 orbits selected at random while estimating the bootstrapped uncertainties.

in the historical radial velocities, which are difficult to quantify, and which may on their own be distorting the shape of the orbit, and imposing that shape on the much less numerous astrometric measurements. For this reason, a solution giving higher weight to the astrometry (Section 5.5) is preferred with a mass of the Cepheid of 5.13 ± 0.28 (5%) M_{\odot} .

Table 5. Orbit Fitting Results..

Parameter	RV Only	Astrometry Only	σ Weights	$N\sigma$ Weights	Replicated
P_{orb} (yr)	29.4330 ± 0.0079	29.49 ± 0.35	29.448 ± 0.012	29.384 ± 0.017	29.416 ± 0.028
T_{peri} (JY)	2016.801 ± 0.011	2016.781 ± 0.049	2016.857 ± 0.012	2016.833 ± 0.017	2016.831 ± 0.044
e	0.6195 ± 0.0015	0.6309 ± 0.0079	0.6290 ± 0.0016	0.6336 ± 0.0235	0.6354 ± 0.0066
ω_{Aa} ($^{\circ}$)	303.04 ± 0.34	305.22 ± 0.95	304.33 ± 0.26	304.46 ± 3.17	304.54 ± 0.84
K_1 (km s^{-1})	3.7409 ± 0.0075		3.738 ± 0.010	3.796 ± 0.311	3.762 ± 0.025
γ (km s^{-1})	-16.084 ± 0.025		-16.0970 ± 0.0047	-16.110 ± 0.170	-16.1024 ± 0.0084
Ω ($^{\circ}$)		202.16 ± 0.94	200.16 ± 0.70	201.20 ± 2.59	201.28 ± 1.18
i ($^{\circ}$)		127.82 ± 0.77	128.57 ± 1.00	127.707 ± 3.191	127.57 ± 1.21
a (mas)		129.07 ± 1.18	127.72 ± 1.85	129.371 ± 5.432	129.55 ± 2.05
Reference	(Torres 2023)	Section 5.2	Section 5.3	Section 5.4	Section 5.5
M_{tot} (M_{\odot})		6.35 ± 0.23	6.16 ± 0.28	6.4153 ± 0.7576	6.45 ± 0.31
M_{Aa} (M_{\odot})			4.87 ± 0.26	5.0864 ± 0.6245	5.13 ± 0.28
M_{Ab} (M_{\odot})			1.295 ± 0.019	1.3289 ± 0.2702	1.316 ± 0.028

NOTE—Masses computed assuming the *Gaia* distance of 136.90 ± 0.34 pc

6. DISCUSSION

6.1. The Cepheid Mass

Approximately three quarters of the 30 year orbit of Polaris has now been observed with *HST*, CHARA, and speckle measurements. The resulting mass of the Cepheid is 5.13 ± 0.28 (5%) M_{\odot} which is larger than before the CHARA and speckle observations were included, but with smaller errors. The previous mass was $3.45 \pm 0.75 M_{\odot}$ (Evans et al. 2018; based on a slightly different distance).

6.2. Cepheid Mass Luminosity Relation

Cepheids provide a quantitative test of evolutionary calculations. In the case of Polaris, the mass derived here is combined with a luminosity to compare with theoretical predictions. For MW Cepheids in general, definitive luminosities will be produced by *Gaia* in the release that includes orbital fits in the analysis. For Polaris, we use the distance to Polaris B as discussed in Section 1.1. Since Polaris B is not a close binary, an orbit is not required in the *Gaia* solution.

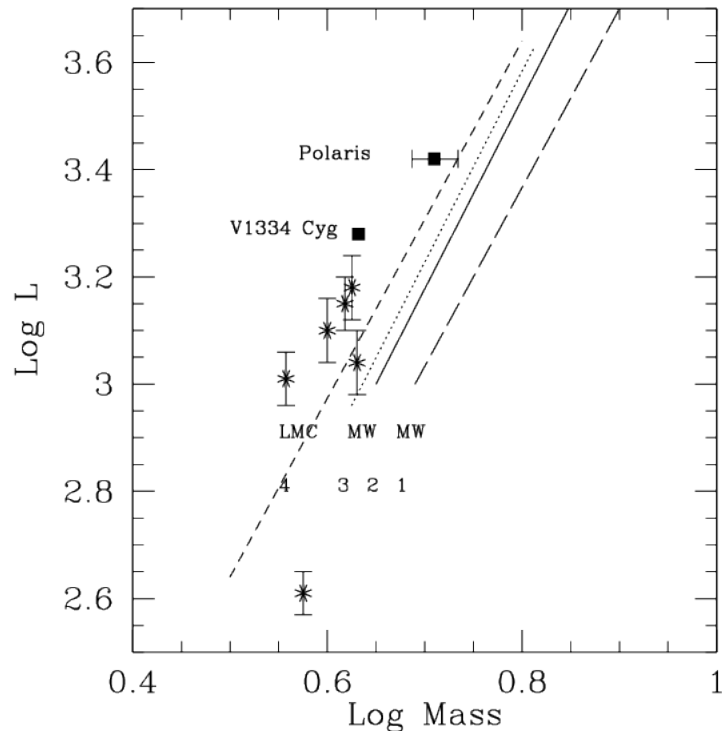


Figure 7. Cepheid mass-luminosity relation. The Milky Way Cepheids, Polaris (this work) and V1334 Cyg (Gallenne et al 2018), are plotted as squares. LMC Cepheids (Pilecki et al 2021) are plotted as asterisks. Overplotted are predictions from evolutionary tracks (Bono et al. 2016; Anderson et al. 2014; Anderson et al. 2016) for (1) long dash: MW metallicity, no main sequence convective overshoot; (2) solid: MW metallicity, moderate convective overshoot; (3) dotted line: MW metallicity, small convective overshoot and rotation; (4) short dash line: LMC metallicity, moderate convective overshoot. Mass and Luminosity are in solar units.

Figure 7 shows the Cepheid mass-luminosity relation with the location of Polaris in comparison with the predictions from evolutionary calculations of several groups, which predict the luminosity for a given mass.

Figure 7 includes V1334 Cyg, which has the most accurate Cepheid mass at present (Gallenne et al 2018). The solution also provides an accurate (3%) distance to the system. It is a good comparison for Polaris since it has similar characteristics. It pulsates in the first overtone, and has a period (luminosity) similar to Polaris. Also shown in Figure 7 are masses for LMC Cepheids in eclipsing binaries from Pilecki et al. (2021). Luminosities for the MW Cepheids are from the distance to Polaris (above) and V1334 Cyg. Luminosities for the LMC Cepheids are from Pilecki et al. (2021). The observed mass-luminosity combinations are compared with evolutionary predictions from Bono et al. (2016) and Anderson et al. (2014). The Bono tracks cover MW and LMC metallicities. For the MW the relations are shown for no main sequence convective core overshoot and moderate overshoot. The Anderson relation is for main sequence rotation and moderate convective overshoot. The lower metallicity of the LMC stars results in a higher luminosity than for solar abundance stars, as indicated by the models.

The determination of the mass of Polaris in this study is part of a series of studies to measure of Cepheids. Additional MW Cepheids are to be added to Figure 7. However the first indication is that in the examples so far (Polaris, V1334 Cyg, and the LMC Cepheids), the luminosity is larger than predicted by current evolutionary calculations.

6.3. Evolutionary Tracks

To explore the details of the calculation results, we provide Figure 8 updated from Figure 7 in Evans et al. (2018). Temperatures are from $(B-V)_0$, as discussed in Evans et al. (2018). Figure 8 illustrates the location of Polaris and also V1334 Cyg with respect to evolutionary calculations for 4, 5, and 7 M_\odot from Georgy et al. (2013). The tracks contrast evolution for stars with zero rotational velocity on the main sequence and those with 0.95 breakup velocity. Both Polaris and V1334 Cyg are more luminous than the 5 M_\odot track in the blue loop, even for large main sequence rotation. For a comparison between codes, Figure 8 in Evans et al. (2018) shows the location of Polaris compared with three sets of tracks for a 5 M_\odot model: Geneva (Georgy et al. 2013), MIST (Choi et al. 2016) and PARSEC¹⁴ (based on the Bressan et al. (2012) group). All three sets of tracks are shown for zero initial main sequence rotation; for the Geneva and MIST calculations, a track is also shown for substantial rotation. In this figure, the MIST tracks (both with and without substantial main sequence rotation) approximately coincide with the Georgy tracks with rotation.

One further criterion for the comparison between observed masses and evolutionary tracks is that Cepheids are found in a region of the Luminosity–Temperature diagram (Figure 8) where the blue loops penetrate the instability strip. This was a motivation of the exploration of the effect of rotation in main sequence progenitors (Anderson et al. 2014), since increasing the main sequence core convective overshoot increases luminosity at the Cepheid phase, but truncates the blue loops. Evolutionary tracks for additional masses probe this further.

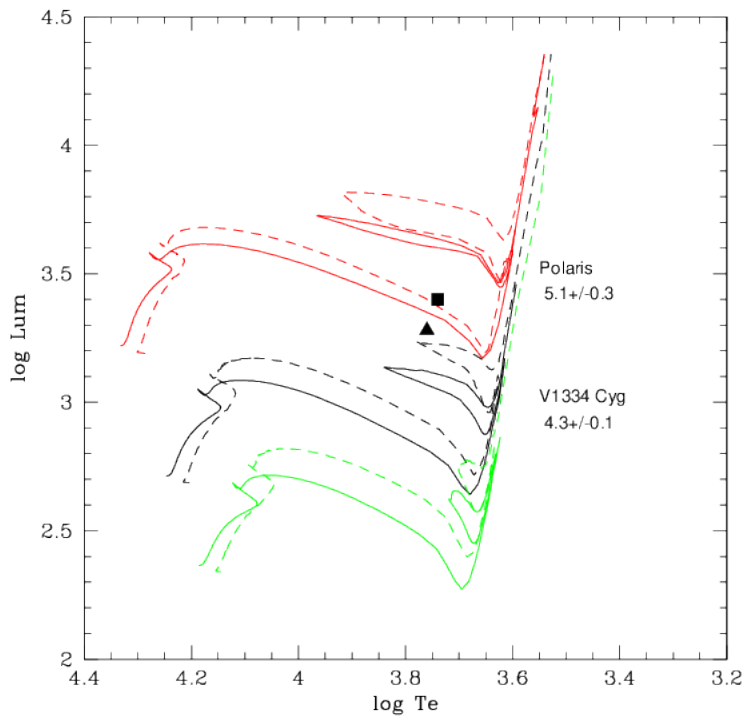


Figure 8. Polaris and V1334 Cyg compared with evolutionary tracks. For Polaris (filled square) and V1334 Cyg (filled triangle) the mass in M_\odot is listed next to the star name. The evolutionary tracks from Georgy et al. (2013) are for 4, 5, and 7 M_\odot in colors of green, black, and red respectively. Solid lines are for zero rotational velocity on the main sequence; dashed lines have 0.95 breakup velocity. Luminosity is in solar units; temperature is in Kelvin.

6.4. Properties of Polaris

¹⁴ http://philrosenfield.github.io/padova_tracks

This study provides astrometry from CHARA interferometry and APO speckle observations for the Polaris Aa and Ab system. When combined with previous *HST* observations and radial velocities (Torres 2023), a mass of $5.13 \pm 0.28 M_{\odot}$ is derived. The observed luminosity for Polaris is brighter than predicted by current evolutionary tracks. The predicted luminosity depends on the rotation of the main sequence progenitor, but Fig 8 shows that Polaris is at least 0.4 mag brighter than the predicted tracks including a small correction from the $5 M_{\odot}$ tracks to the mass of Polaris (based on 0.5 critical breakup velocity [Anderson et al. 2014]). This study is part of a series of studies of Cepheid masses using interferometry as well as *Gaia* astrometry to examine this questions.

In the case of Polaris several of its properties are unusual in the context of Cepheids. It pulsates in the first overtone, which may be linked with the rapid period change. Overtone pulsators have more instability in their pulsation periods, which can sometimes be interpreted as rapid period change. The variation in pulsation amplitude may also be related to its pulsation mode. The recent discussion of velocities (Torres 2023) postulates that the “glitch” in pulsation may occur at periastron passage. This would add a new factor to the interpretation of the observations. It has been suggested for other Cepheids with a “phase jump” that they are likely to be binary systems (Csonyeyi et al. 2022). In summary, while these properties are unusual for Cepheids, they exist in other stars. Thus Polaris fits in the framework of pulsating supergiants, particularly if orbital motion is included. While these characteristics complicate the interpretation of observations, all are found in stars without abnormal evolution.

The identification of star spots is consistent with several properties of Polaris. It has a very low pulsation amplitude, which sets it apart from full amplitude Cepheids. This may mean that the atmosphere is like that of a nonvariable supergiant, which have often indicators of activity. It is not clear how full amplitude pulsation affects the atmosphere and magnetic field in pulsators, so Polaris is an interesting test case.

Polaris has a couple of other characteristics which would be consistent with magnetically related spots. Polarization has been found (Barron et al. 2022). However, the polarization measurements look more like those of the nonvariable supergiant α Per than other Cepheids (Grunhut et al. 2010), but this may just reflect the very low pulsation amplitude. Polaris has also been detected in X-rays (Evans et al. 2022).

Our identification of star spots opens the prospect of determining a rotation period. It also can explain why additional periodicities have been difficult to find, since the distribution of spots is variable. The long period ($\simeq 120$ day) variation found by Lee et al. (2008), for instance, might be a rotation period. 40 and 60 d periods found by Anderson (2019) may be related.

Another possible interpretation of surface features on Polaris is convective supergranules as discussed by Schwarzschild (1975).

A final characteristic of the orbit of Polaris is the high eccentricity. This is often found in systems which have undergone three body interaction, which would be consistent with the Cepheid being a merger product from a former triple system, as suggested by Evans, et al (2018). However, high eccentricity is frequently found in long period systems (Shetye et al. 2024) so it does not require special conditions.

7. SUMMARY AND FUTURE WORK

The CHARA and APO observations of the Polaris Aa and Ab system have added to previous astrometric observations to cover approximately three quarters of the orbit. The mass of the Cepheid which results from these data and the spectroscopic orbit is 5.13 ± 0.28 (5%) M_{\odot} . The Cepheid is overluminous for this mass according to current calculations. Starspots have been identified in the CHARA images, providing another tool to use to investigate the Cepheid.

Further observations with CHARA and APO will provide additional coverage of the orbit and add to the determination of the mass.

This work is based upon observations obtained with the Georgia State University Center for High Angular Resolution Astronomy Array at Mount Wilson Observatory. The CHARA Array is supported by the National Science Foundation under Grant No. AST-1636624 and AST-2034336. Institutional support has been provided from the GSU College of Arts and Sciences and the GSU Office of the Vice President for Research and Economic Development. Time at the CHARA Array was granted through the NOIRLab community access program (NOIRLab PropID: 2018B-0039; PI: N. Evans). PK acknowledges funding from the European Research Council (ERC) under the European Union’s Horizon 2020 research and innovation program (project UniverScale, grant agreement 951549). SK acknowledges funding for MIRC-X from the European Research Council (ERC) under the European Union’s Horizon 2020 research and innovation programme (Starting Grant No. 639889 and Consolidated Grant No. 101003096). JDM acknowledges funding for the development of MIRC-X (NASA-XRP NNX16AD43G, NSF-AST 1909165). AG acknowledges the

support of the Agencia Nacional de Investigación Científica y Desarrollo (ANID) through the FONDECYT Regular grant 1241073. RMR acknowledges funding from the Heising-Simons Foundation 51 Pegasi b Fellowship. Support was provided to NRE by the Chandra X-ray Center NASA Contract NAS8-03060. This research has received support from the European Research Council (ERC) under the European Union’s Horizon 2020 research and innovation programme (Grant Agreement No. 947660). RIA is funded by the Swiss National Science Foundation through an Eccellenza Professorial Fellowship (award PCEFP2_194638). This research is based on observations made with the Mercator Telescope, operated on the island of La Palma by the Flemish Community, at the Spanish Observatorio del Roque de los Muchachos of the Instituto de Astrofísica de Canarias (observations from Anderson et al.). Hermes is supported by the Fund for Scientific Research of Flanders (FWO), Belgium, the Research Council of K.U. Leuven, Belgium, the Fonds National de la Recherche Scientifique (F.R.S.- FNRS), Belgium, the Royal Observatory of Belgium, the Observatoire de Genève, Switzerland, and the Thüringer Landessternwarte, Tautenburg, Germany.

This work has made use of data from the European Space Agency (ESA) mission *Gaia* (<https://www.cosmos.esa.int/gaia>), processed by the *Gaia* Data Processing and Analysis Consortium (DPAC, <https://www.cosmos.esa.int/web/gaia/dpac/consortium>). Funding for the DPAC has been provided by national institutions, in particular the institutions participating in the *Gaia* Multilateral Agreement. This research made use of services provided by the Jean-Marie Mariotti Center (Aspro, SearchCal, and OIBD). The SIMBAD database, and NASA’s Astrophysics Data System Bibliographic Services were used in the preparation of this paper.

The software used in this project is available from Squeeze [10.5281/zenodo.11643362] and ROTIR [10.5281/zenodo.11643362]]<https://doi.org/DOI>.

REFERENCES

- Anderson, R. I., et al. 2014, *A&A*, 564, 100
 Anderson, R. I. 2016, *A&A*, 591, A8
 Anderson, R. I. 2018, *A&A*, 611, L7
 Anderson, R. I. 2019, *A&A*, 623, A146
 Anderson, R. I., Viviani, G., Shetye, S., et al. 2024, in press
 Anugu, N., Le Bouquin, J.-B., Monnier, J. D., et al. 2020, *AJ*, 160, 158
 Arellano Ferro, A 1983, *ApJ*, 274, 755
 Baron, F. 2020, *Proc. SPIE*, 11446, 114461N
 Baron, F., Kloppenborg, B., & Monnier, J. 2012, *Proc. SPIE*, 8445, 84451D
 Baron, F., Monnier, J. D., & Kloppenborg, B. 2010, *Proc. SPIE*, 7734, 77342I
 Barron, J. A., Wade, G. A., Evans, N. R., Folsom, C. P. and Neilson, H. R. 2022, *MNRAS*, 512, 4021
 Berdnikov, L. N. and Pastukhova, E. N. 1995, *Astronomy Letters*, 21 369
 Bond, H. E., Nelan, E. P., Evans, N. R., Schaefer, G. H. and Harmer, D. 2018, *ApJ*, 853, 55
 Bonneau, D., Delfosse, X., Mourard, D., et al. 2011, *A&Ap*, 535, A53
 Bono, G., Braga, V. F., Pietrinferni, A., et al. 2016, *MmSAI*, 87, 358
 Bono, G., et al. 2001, *MNRAS*, 325, 1353
 Bourgés, L., Lafrasse, S., Mella, G, et al. 2014, *ASPC*, 485, 223
 Bressan, A., Marigo, P., Girardi, L., et al. 2012, *MNRAS*, 427, 127
 Bruntt, H., Evans, N. R., Stello, D. et al. 2008, *ApJ*, 683, 433
 Chawla, N. V., Bowyer, K. W., Hall, L. O., Kegelmeyer, W. P. 2002, *Journal of Artificial Intelligence Research*, 16, 321
 Choi, J., Dotter, A., Conroy, C., Cantillo, M., Paxton, B., and Johnson, B. D. 2016, *ApJ*, 823, 102
 Claret, A., & Bloemen, S. 2011, *A&Ap*, 529, A75
 Csoranyi, G., Szabados, L., Molnar, L. et al. 2022, *MNRAS*, 511, 2125
 Davidson, Jr., J. W., Horch, E. P., Majewski, S. R. et al. 2024, *AJ*, accepted
 Engle, S. G., Guinan, E. F., and Harmanec, P. 2018, *RNAAS*, 2,3
 Evans, N. R., Schaefer, G. H., Bond, H. E. et al. 2008, *ApJ*, 136, 1137
 Evans, N. R., Karovska, M., Bond, H. E., et al. 2018, *ApJ*, 863, 187
 Evans, N. R., Engle, S., Pillitteri, I., et al. 2022, *ApJ*, 938, 153
 Feast, M. W. and Catchpole, R. M. 1997, *MNRAS*, 286, 11
 Foreman-Mackey, D., Hogg, D. W., Lang, D., & Goodman, J. 2013, *PASP*, 125, 306
Gaia Collaboration, Vallenari, A., Brown, A. G. A., et al. 2023, *A&Ap*, 674, A1
 Gallenne, A., Mérand, A., Kervella, P., et al. 2015, *A&Ap*, 579, A68
 Gallenne, A., Kervella, P., Evans, N. R., et al. 2018, *ApJ*, 867, 121,
 Gallenne, A., Pietrzyński, G., Graczyk, D., et al. 2019a, *A&Ap*, 632, A31
 Gallenne, A., Kervella, P., Borgniet, S., et al. 2019b, *A&Ap*, 622, A164
 Georgy, C., Ekstrom, S., Granada, A., Meynet, G., Mowlavi, N., Eggenberger, P. and Maeder, A. 2013, *A&A*, 553, 24
 Grunhut, J. H., Wade, G. A., Hanes, D. A., abd Alecian, E. 2010, *MNRAS*, 408, 2290
 Hanbury Brown, R., Davis, J., Lake, R. J. W., & Thompson, R. J. 1974, *MNRAS*, 167, 475
 Heintz, W. D. 1978, *Double Stars* (Reidel: Dordrecht)
 Horch, E. P., Veillette, D. R., Gallé, R. et al 2009, *AJ*, 137, 5057
 Horch, E. P., Ninkov, Z., and Slawson, R. W. 1997, *AJ*, 114, 2117
 Kamper, K. W. 1996, *JRASC*, 90, 140
 Kamper, K. W. and Fernie, J. D. 1998, *AJ*, 116, 936
 Khan, S., Anderson, R. I., Miglio, A., Mosser, B., and Elsworth, Y. P. 2023, *A&A*, 680, A105
 Kurtz, D. 2022, *ARAA*, 60, 31
 Lee, B.-C., Mkrtychian, D. E., Han, I., et al. 2008, *AJ*, 135, 2240
 Lindegren, L., Bastian, U., Biermann, M., et al. 2021, *A&A*, 649, A4
 Markwardt, C. B. 2009, in *ASP Conf. Ser.*, Vol. 411, *Astronomical Data Analysis Software and Systems XVIII*, ed. D. A. Bohlender, D. Durand, & P. Dowler (San Francisco, CA: ASP), 251

Mérand, A. 2022, Proc. SPIE, 12183, 12183N
 Mérand, A., Kervella, P., Breielfelder, J., et al. 2015, A&A, 584A, 80
 Mérand, A., Kervella, P., Coudé du Foresto, V., et al. 2006, A&A, 453, 155
 Monnier, J. D., Berger, J.-P., Millan-Gabet, R., & ten Brummelaar T. A. 2004, in SPIE Conference Series, ed. W. A. Traub, Vol. 5491, 1370
 Monnier, J. D., Zhao, M., Pedretti, E., et al. 2007, Science, 317, 342
 Monnier, J. D., Che, X., Zhao, M., et al. 2012, ApJ, 761, L3
 Moskalik, P. & Gorynya, N. A. 2005 AcA, 55, 247
 Neilson, H. R. et al. 2011, A&A, 529, L9
 Neilson, H. R., Engle, S. G., Guinan, D., Langer, N., Wasatonic, R. P., and Williams, D. B. 2012, ApJ, 745, L32
 Pilecki, B., et al. 2018, ApJ, 862,43
 Pilecki, B., Pietrzyński, G., Anderson, R. I., et al. 2021, ApJ, 910, 118
 Riess, A. G., Casertano, S., Yuan, W., et al. 2021, ApJ, 908, L6
 Roemer, E. 1965, ApJ, 141, 1415
 Roettenbacher, R. M., Monnier, J. D., Korhonen, H., et al. 2016, Nature, 533, 217

Schaefer, G. H., Hummel, C. A., Gies, D. R. et al. 2016, AJ, 152, 213
 Schwarzschild, M. 1975, ApJ, 195, 137
 Shetye, S. S., Anderson, R. I., Viviani, G., Mowlavi, N. Eyer, L., Evans, N. R., and Szabados, L. 2024, A&A, submitted
 Szabados, L. 1989, Commun. Konkoly Obs. Hungary, 94, 1
 Szabados, L. 1991, Commun. Konkoly Obs. Hungary, 96, 123
 Szabados L., 1992, in McAlister H. A., Hartkopf W. I., eds, ASP Conf. Ser. Vol. 32, IAU Colloq. 135: Complementary Approaches to Double and Multiple Star Research. Astron. Soc. Pac., San Francisco, p. 255
 ten Brummelaar, T. A., McAlister, H. A., Ridgway, S. T., et al. 2005, ApJ, 628, 453
 Torres, G. 2023, MNRAS, 526, 2510
 Turner, D. G., Savoy, J., Derrah, J., Abdel-Latif, M. A., and Berdnikov, L. N. 2005, PASP, 117, 207
 van Leeuwen, F. 2007, A&Ap, 474, 653
 van Leeuwen, F. 2013, A&Ap, 550, L3
 Wielen, R., Jahreiss, H., Dettbarn, C., Lenhardt, H., and Schwan, H. 2000, A&A, 360, 399

APPENDIX

A. INTERFEROMETRIC DATA PLOTS - IMAGING RESULTS

Figure Set 12.1 shows the visibilities and closure phases measured with CHARA MIRC-X averaged over 10-minute observing sets. The data (black circles) and observables extracted from the reconstructed images (red circles) are plotted in the top panels of each figure. The bottom panels show the residuals between the data and the image.

Fig. Set 12. Imaging Results

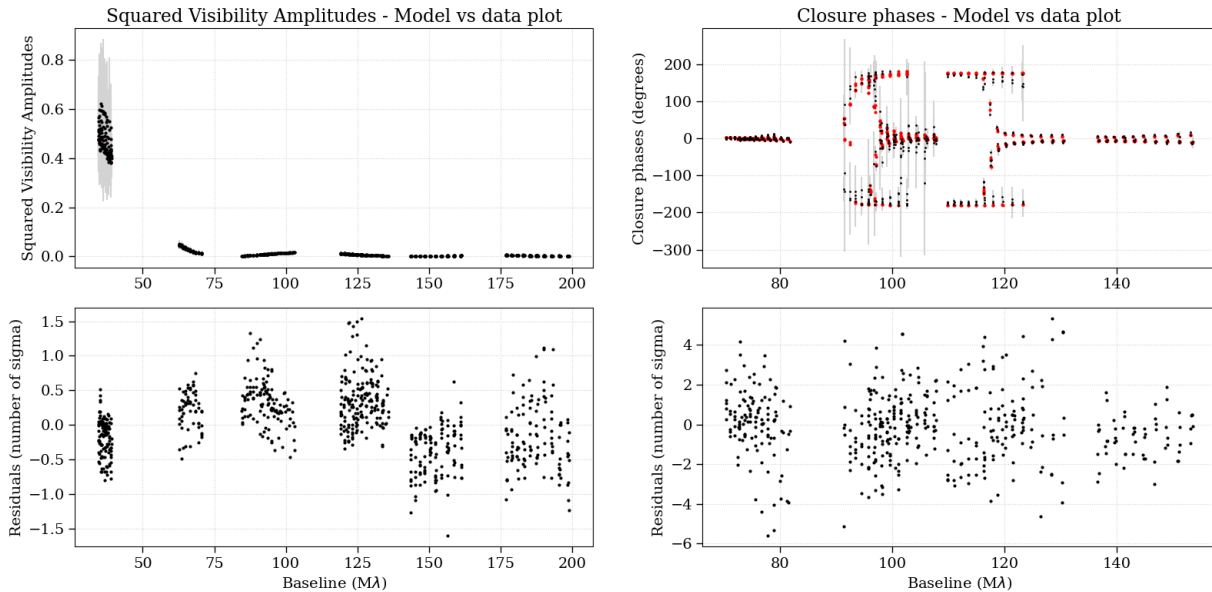


Figure 12.1. Visibilities and closure phases measured with CHARA MIRC-X and averaged over 10-minute observing sets for Polaris on UT 2018Aug27. The black symbols are the measured values while the red symbols are extracted from the ROTIR reconstructed image. The lower panels show the residuals between the data and the image. The complete set of figure set (4 images) is available in the online journal.

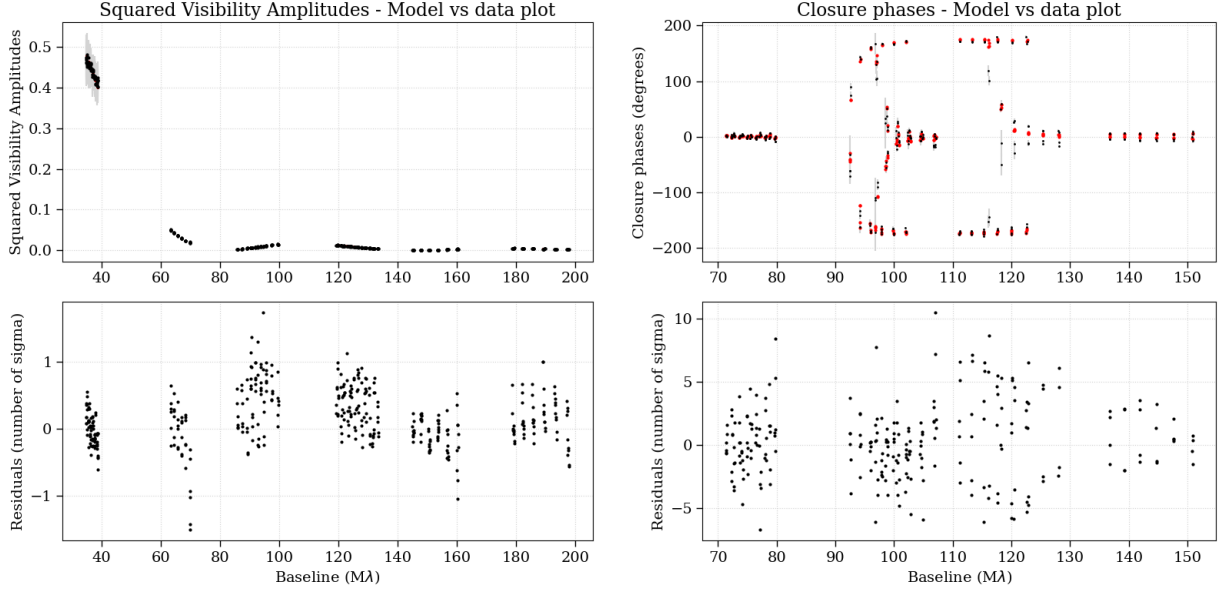


Figure 12.2. Visibilities and closure phases measured with CHARA MIRC-X and averaged over 10-minute observing sets for Polaris on UT 2019Apr09. The black symbols are the measured values while the red symbols are extracted from the ROTIR reconstructed image. The lower panels show the residuals between the data and the image.

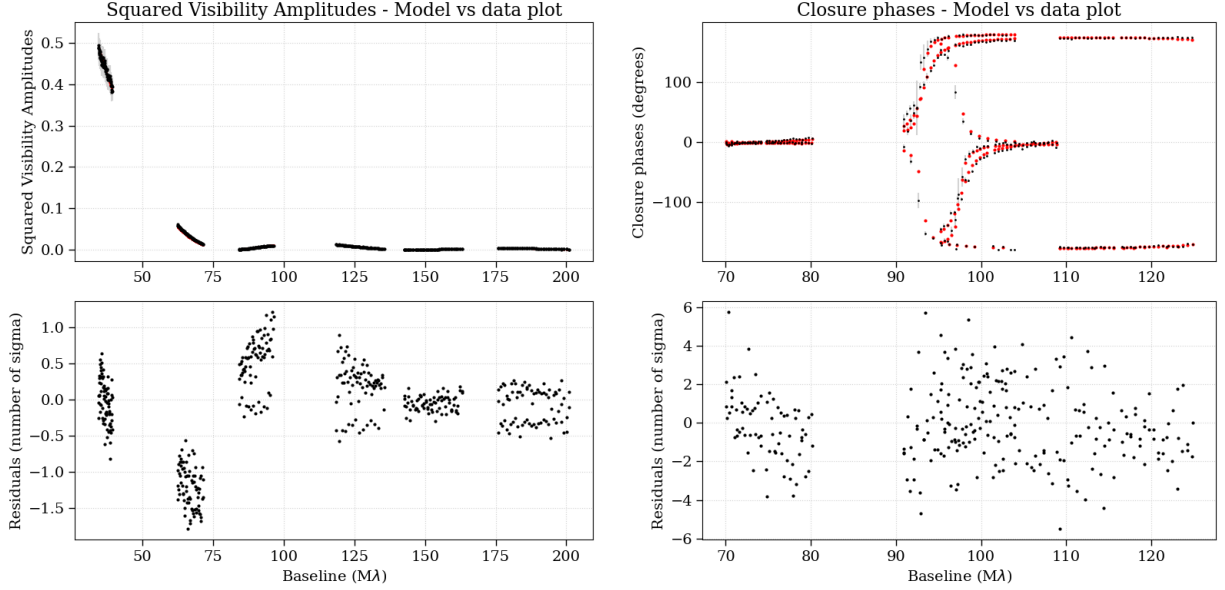


Figure 12.3. Visibilities and closure phases measured with CHARA MIRC-X and averaged over 10-minute observing sets for Polaris on UT 2019Sep02. The black symbols are the measured values while the red symbols are extracted from the ROTIR reconstructed image. The lower panels show the residuals between the data and the image.

B. INTERFEROMETRIC DATA PLOTS - BINARY FITS

Figure Set 13.1 shows the results from the binary fits to the CHARA MIRC-X interferometry using the 30 second integration time. Each figure shows the (u, v) coverage, the χ^2 map from the binary grid search, the visibilities, and the closure phases. The χ^2 maps are centered at the predicted location based on the updated orbit fit. The nights with reliable detections show a clear minimum in the χ^2 indicated by the colored circles. The nights with unreliable binary fits show more ambiguity in the χ^2 maps.

Fig. Set 13. Binary Fits

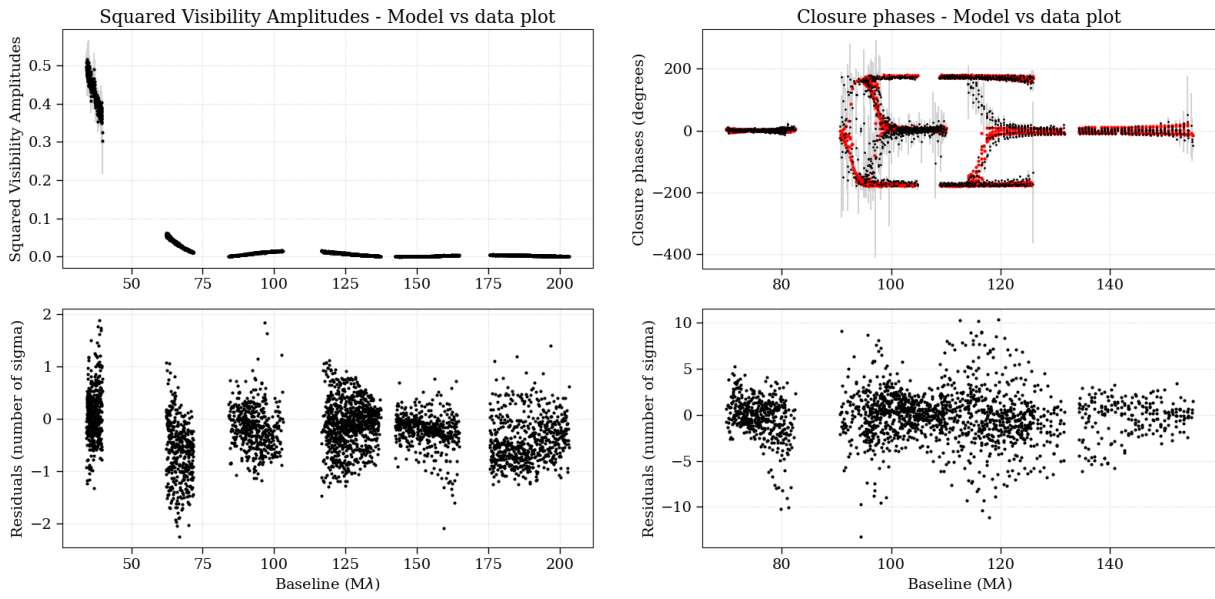


Figure 12.4. Visibilities and closure phases measured with CHARA MIRC-X and averaged over 10-minute observing sets for Polaris on UT 2021Apr02, 2021Apr03, and 2021Apr04. The black symbols are the measured values while the red symbols are extracted from the ROTIR reconstructed image. The lower panels show the residuals between the data and the image.

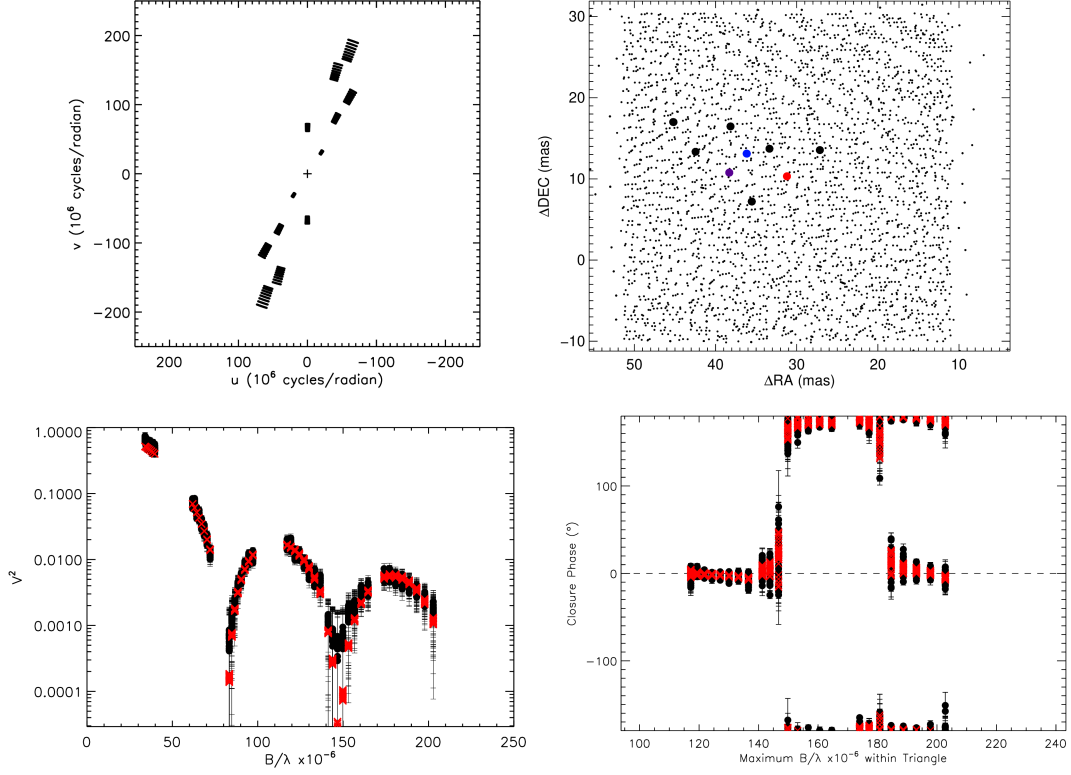


Figure 13.1. Binary fit for Polaris on UT 2016Sep12. Top Row: (u, v) coverage (left) and χ^2 map from the binary grid search (right). In the χ^2 map, the red, orange, yellow, green, blue, purple, large black, and small black symbols correspond to solutions within $\Delta\chi^2 = 1, 4, 9, 16, 25, 36, 49,$ and >50 from the minimum χ^2 . Bottom row: The filled black circles show the squared visibilities (left) and closure phases (right) measured with MIRC-X using the 30 second integration time. The red crosses show the best-fit binary model. The complete set of figure set (8 images) is available in the online journal.

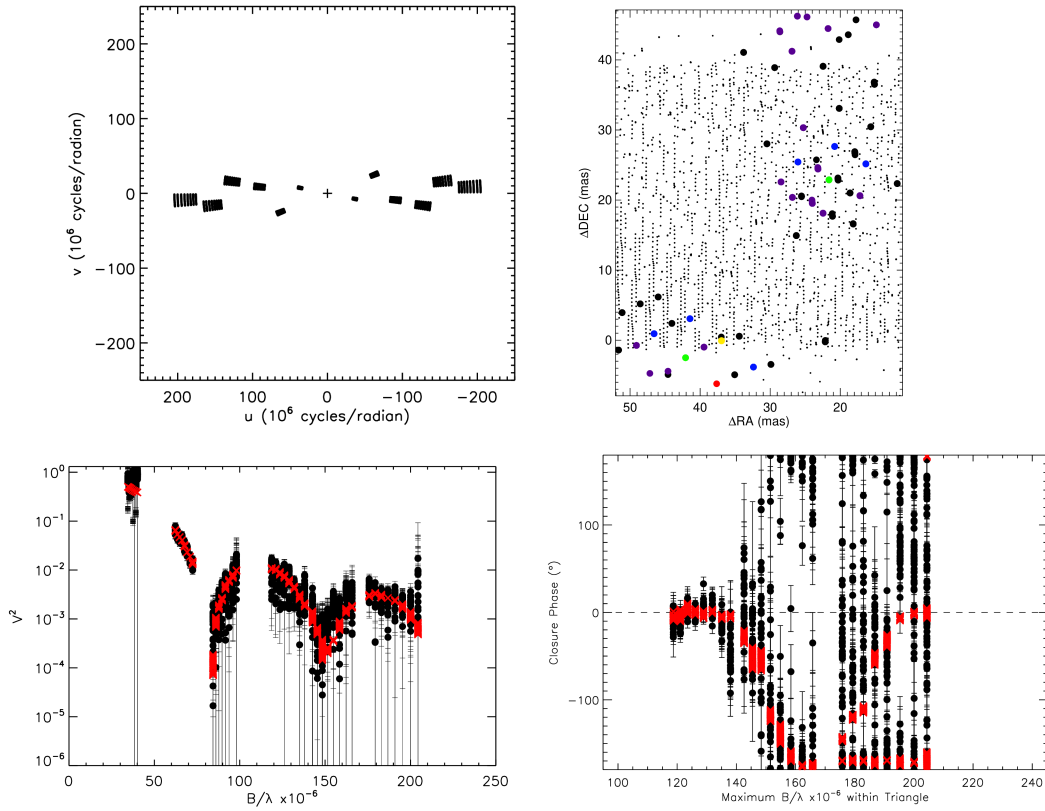


Figure 13.2. Binary fit for Polaris on UT 2016Nov18. Top Row: (u, v) coverage (left) and χ^2 map from the binary grid search (right). In the χ^2 map, the red, orange, yellow, green, blue, purple, large black, and small black symbols correspond to solutions within $\Delta\chi^2 = 1, 4, 9, 16, 25, 36, 49,$ and >50 from the minimum χ^2 . Bottom row: The filled black circles show the squared visibilities (left) and closure phases (right) measured with MIRC-X using the 30 second integration time. The red crosses show the best-fit binary model.

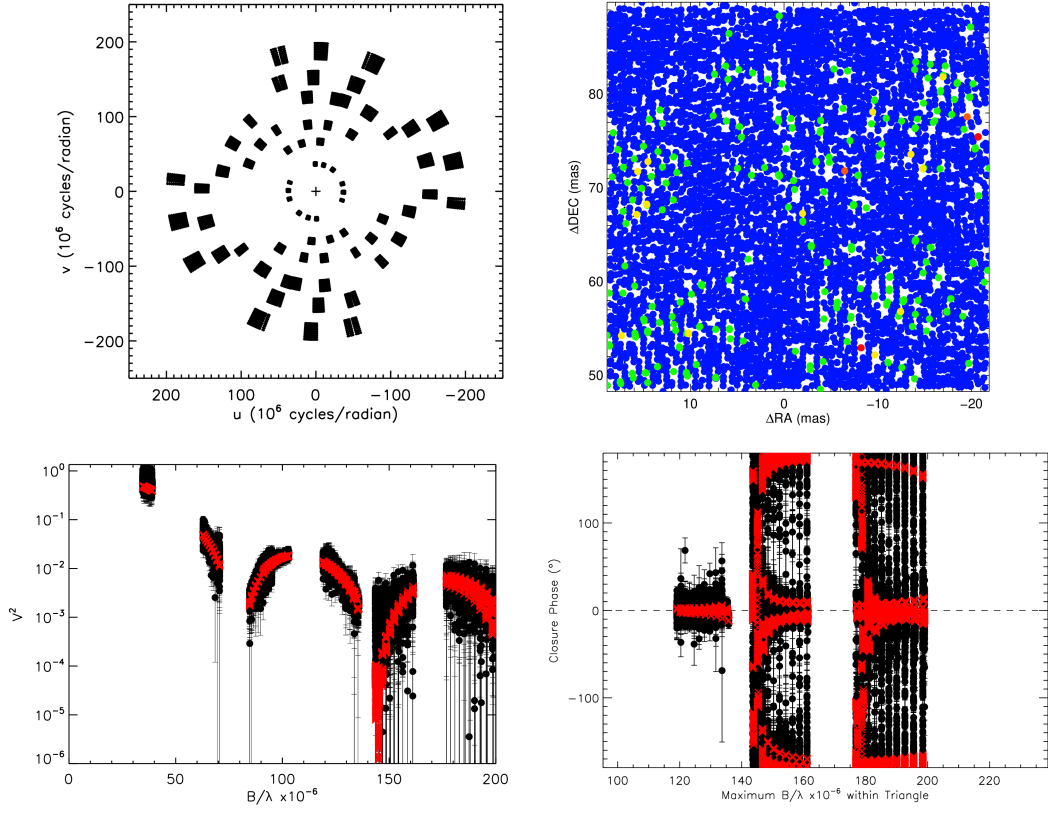


Figure 13.3. Binary fit for Polaris on UT 2018Aug27. Top Row: (u, v) coverage (left) and χ^2 map from the binary grid search (right). In the χ^2 map, the red, orange, yellow, green, blue, purple, large black, and small black symbols correspond to solutions within $\Delta\chi^2 = 1, 4, 9, 16, 25, 36, 49,$ and >50 from the minimum χ^2 . Bottom row: The filled black circles show the squared visibilities (left) and closure phases (right) measured with MIRC-X using the 30 second integration time. The red crosses show the best-fit binary model.

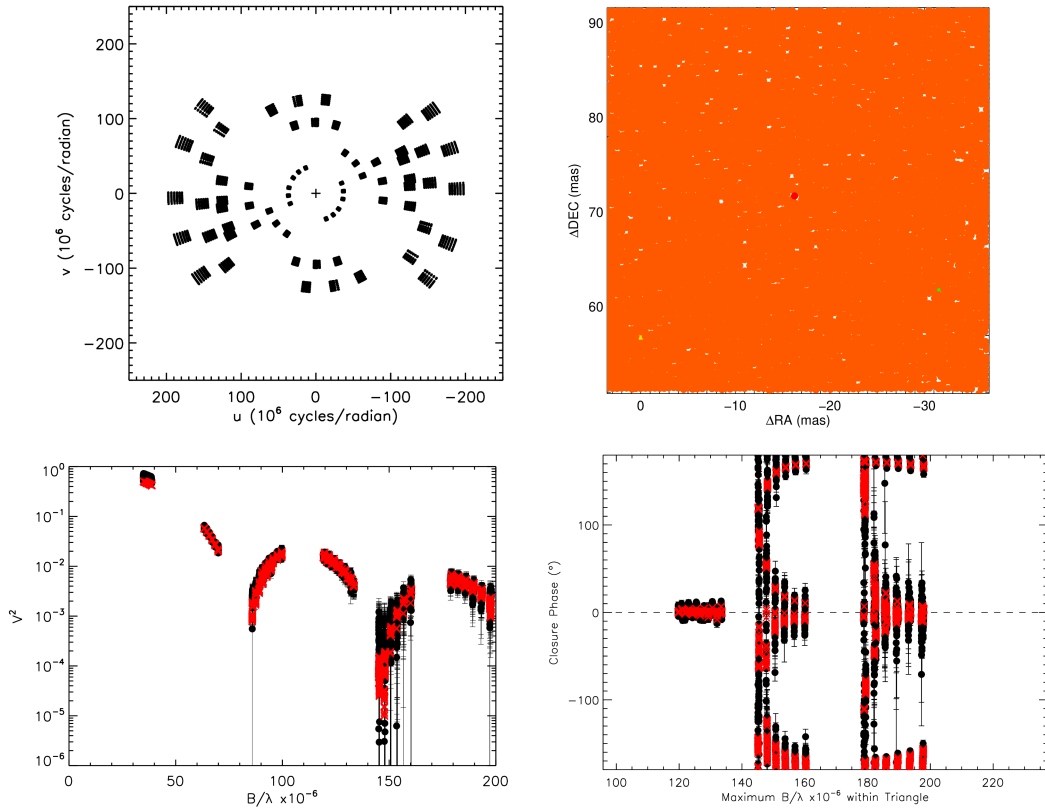


Figure 13.4. Binary fit for Polaris on UT 2019Apr09. Top Row: (u, v) coverage (left) and χ^2 map from the binary grid search (right). In the χ^2 map, the red, orange, yellow, green, blue, purple, large black, and small black symbols correspond to solutions within $\Delta\chi^2 = 1, 4, 9, 16, 25, 36, 49,$ and >50 from the minimum χ^2 . Bottom row: The filled black circles show the squared visibilities (left) and closure phases (right) measured with MIRC-X using the 30 second integration time. The red crosses show the best-fit binary model.

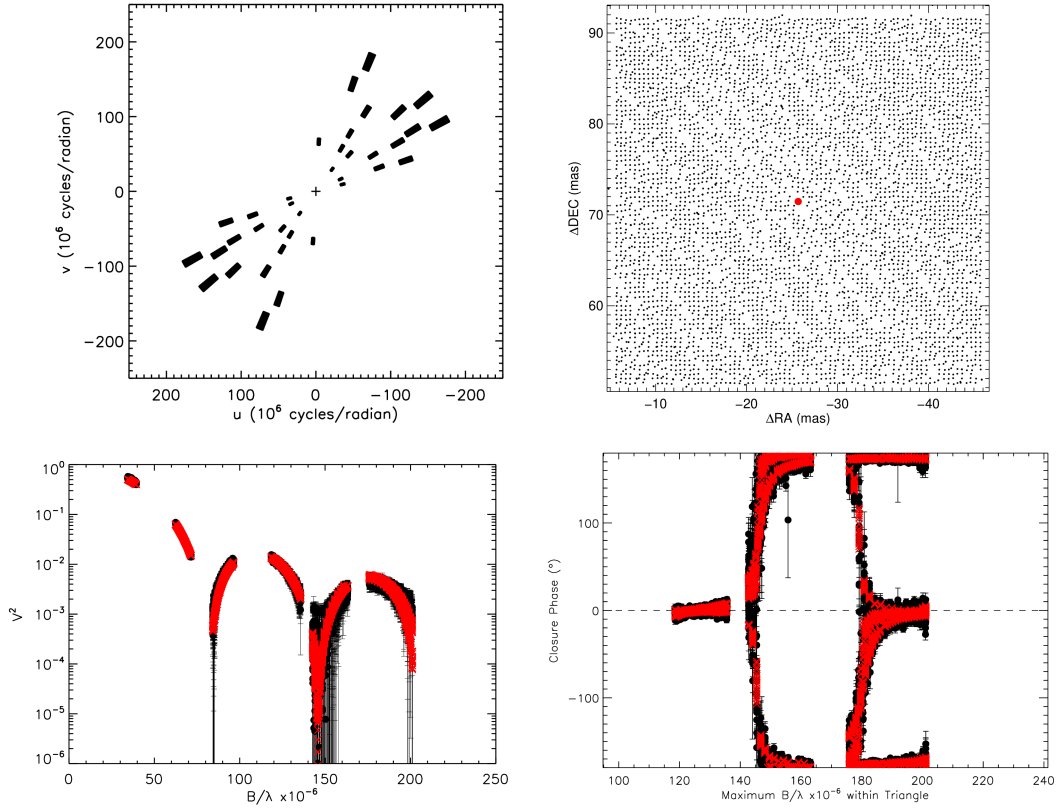


Figure 13.5. Binary fit for Polaris on UT 2019Sep02. Top Row: (u, v) coverage (left) and χ^2 map from the binary grid search (right). In the χ^2 map, the red, orange, yellow, green, blue, purple, large black, and small black symbols correspond to solutions within $\Delta\chi^2 = 1, 4, 9, 16, 25, 36, 49,$ and >50 from the minimum χ^2 . Bottom row: The filled black circles show the squared visibilities (left) and closure phases (right) measured with MIRC-X using the 30 second integration time. The red crosses show the best-fit binary model.

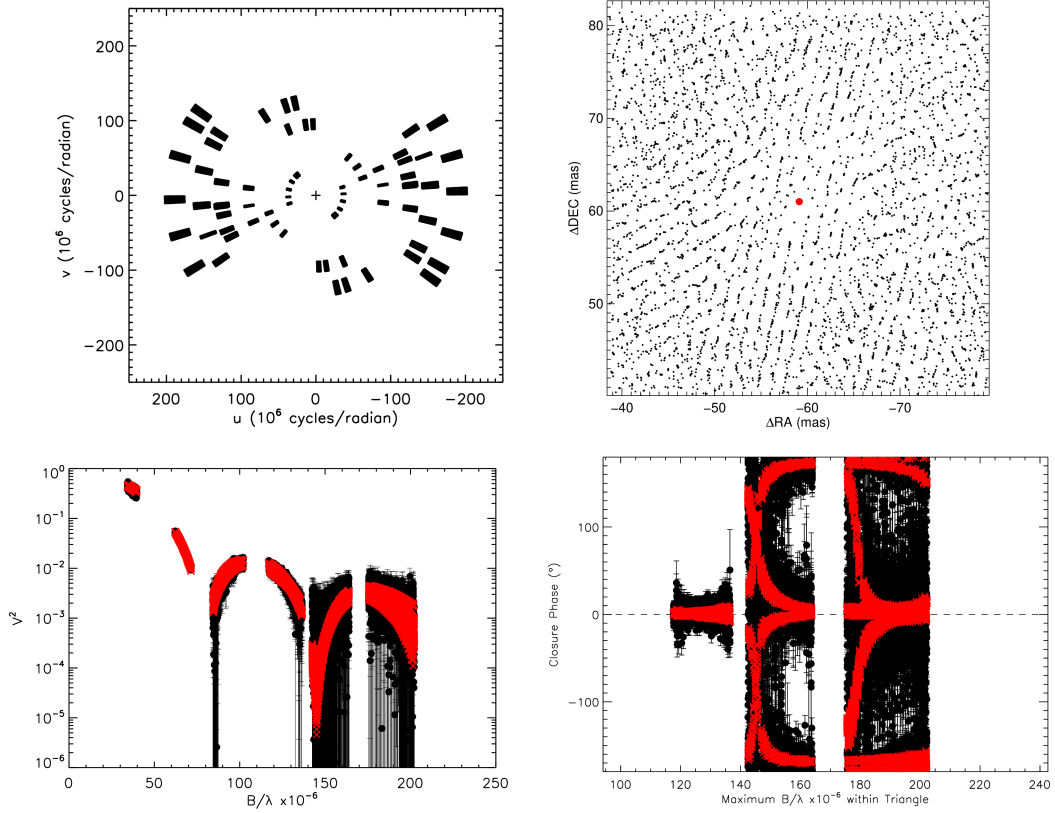


Figure 13.6. Binary fit for Polaris on UT 2021Apr02. Top Row: (u, v) coverage (left) and χ^2 map from the binary grid search (right). In the χ^2 map, the red, orange, yellow, green, blue, purple, large black, and small black symbols correspond to solutions within $\Delta\chi^2 = 1, 4, 9, 16, 25, 36, 49,$ and >50 from the minimum χ^2 . Bottom row: The filled black circles show the squared visibilities (left) and closure phases (right) measured with MIRC-X using the 30 second integration time. The red crosses show the best-fit binary model.

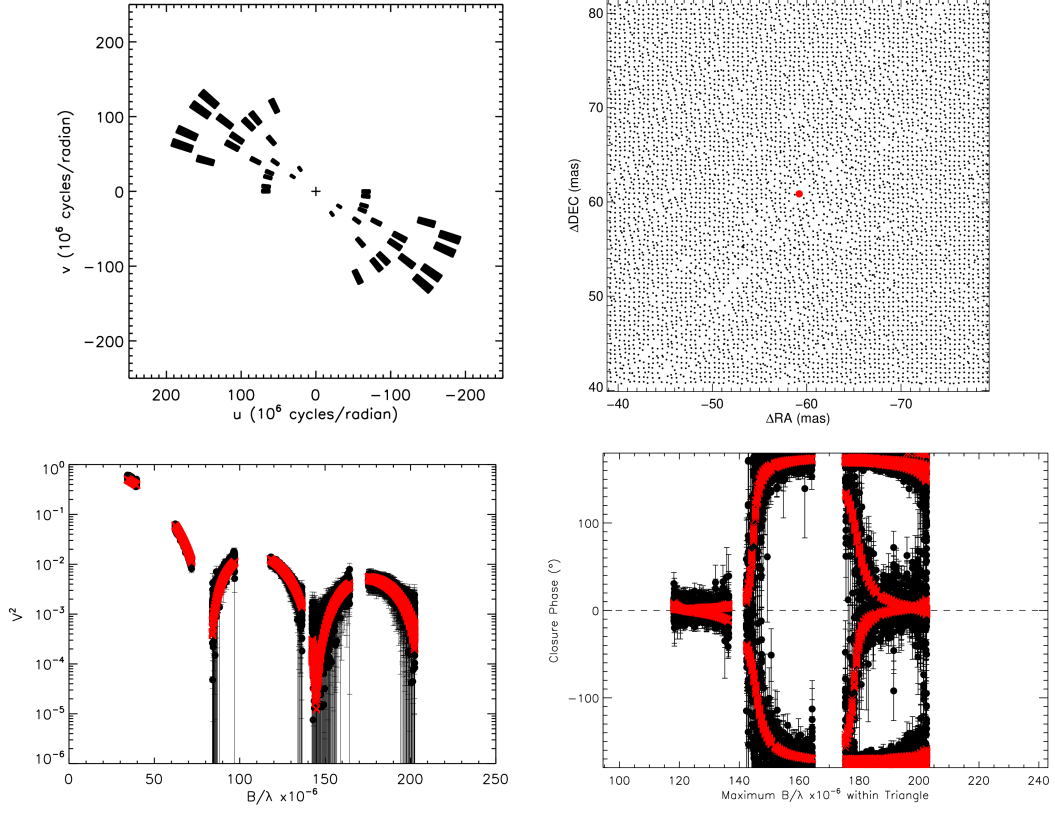


Figure 13.7. Binary fit for Polaris on UT 2021Apr03. Top Row: (u, v) coverage (left) and χ^2 map from the binary grid search (right). In the χ^2 map, the red, orange, yellow, green, blue, purple, large black, and small black symbols correspond to solutions within $\Delta\chi^2 = 1, 4, 9, 16, 25, 36, 49,$ and >50 from the minimum χ^2 . Bottom row: The filled black circles show the squared visibilities (left) and closure phases (right) measured with MIRC-X using the 30 second integration time. The red crosses show the best-fit binary model.

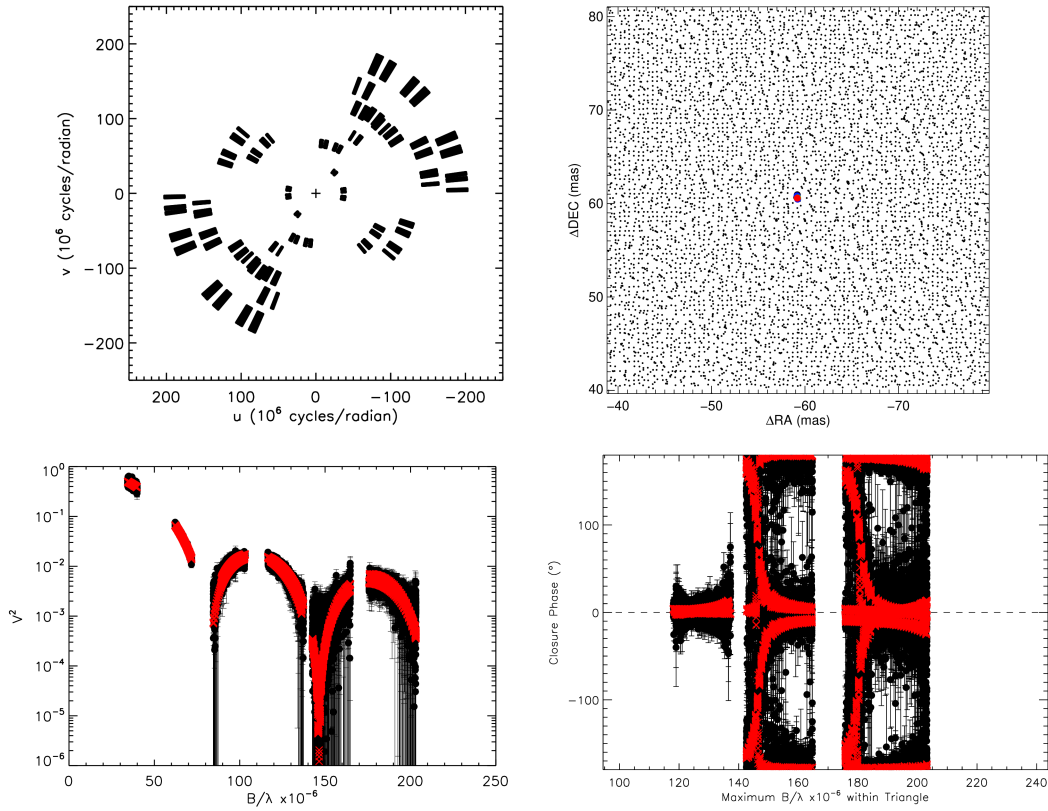


Figure 13.8. Binary fit for Polaris on UT 2021Apr04. Top Row: (u, v) coverage (left) and χ^2 map from the binary grid search (right). In the χ^2 map, the red, orange, yellow, green, blue, purple, large black, and small black symbols correspond to solutions within $\Delta\chi^2 = 1, 4, 9, 16, 25, 36, 49,$ and >50 from the minimum χ^2 . Bottom row: The filled black circles show the squared visibilities (left) and closure phases (right) measured with MIRC-X using the 30 second integration time. The red crosses show the best-fit binary model.